Towards simulating 2D effects in lattice gauge theories on a quantum computer

by

Daniel Paulson

A thesis
presented to the University of Waterloo
in fulfillment of the
thesis requirement for the degree of
Master of Science
in
Physics (Quantum Information)

Waterloo, Ontario, Canada, 2020

Author's Declaration

This thesis consists of material all of which I authored or co-authored: see Statement of Contributions included in the thesis. This is a true copy of the thesis, including any required final revisions, as accepted by my examiners.

I understand that my thesis may be made electronically available to the public.

Statement of Contributions

This thesis was written under the supervision of Prof. Christine Muschik and Prof. Raymond Laflamme, and consists of one manuscript written for publication of which I am the lead author. Dr. Luca Dellantonio edited and contributed to all chapters of this thesis. Further exceptions to sole authorship of material are as follows:

Chapter 1:

Prof. Christine Muschik was the lead author of Chapter 1, with additional contributions from Dr. Jan F. Haase, Dr. Luca Dellantonio, Prof. Karl Jansen, and Prof. Alessio Celi. I contributed to the structure, prose, and editing of this chapter.

Chapter 2:

I authored this entire chapter with help from Prof. Alessio Celi and Prof. Karl Jansen with the derivations presented in Sec. 2.3.

Chapter 3:

I authored this entire chapter, and Prof. Alessio Celi provided the topological term interpretation of the negative fermion mass presented in the footnote of Sec. 3.1. Prof. Karl Jansen provided the basis for the high energy physics background information and motivation presented in Sec. 3.2.

Chapter 5:

I authored this entire chapter, and Dr. Jan F. Haase and Dr. Luca Dellantonio developed the classical optimization routine, and provided the numerical simulation data presented in this chapter.

Chapter 6:

I provided the structure, prose, and editing of this chapter with help from Prof. Christine Muschik.

Abstract

Quantum Field Theories (QFTs) are the most successful theories for describing nature at its most fundamental level. Despite the fact that QFTs are capable of predicting a wide range of phenomena, obtaining solutions to QFTs in parameter regimes where perturbation theory cannot be applied remains a challenge. We propose an experimental scheme to perform quantum simulations of two-dimensional Abelian lattice gauge theories using contemporary quantum devices, paving the way to reach beyond the capabilities of classical simulations. We consider quantum electrodynamics and examine the basic building block of the two-dimensional lattice to study non-trivial magnetic field effects, which are absent in one-dimensional systems. By imposing periodic boundary conditions, we extend the scope of our work to include an infinite 2D structure. Our protocol uses a variational quantum-classical approach to relax the hardware requirements for capturing the intricate many-body interactions that naturally arise in the formulation of gauge-invariant effective field theories. Although we remain platform-independent, we also provide a detailed example of implementation on state-of-the-art trapped ion quantum devices, which can be generalized to other platforms. The techniques for simulating QFTs presented here, combined with advancements in quantum hardware, pose the potential to address longstanding questions in high energy physics.

Acknowledgements

Table of Contents

Chapter 1

Introduction

Gauge theories describe fundamental particle interactions. While current numerical simulations of gauge theories led to several breakthroughs [1, 2], they are ultimately restricted in their predictive capabilities due to the current limitations of classical computers to simulate quantum properties, and in particular due to the infamous sign problem [3, 4]. These crucial limitations call for new methods. Classical tensor network calculations [5, 6] have demonstrated their potential for models in one spatial dimension, but extensions to two and three spatial dimensions face hard numerical problems that still remain unsolved. Quantum simulations provides a powerful toolbox to tackle these challenges and exciting proof-of-concept demonstrations in simulating one-dimensional (1D) physics in gauge theories [7–16] have been achieved. Extending quantum simulations of fundamental particle interactions to higher spatial dimensions, will be crucial to simulate nature and represent an enormous scientific opportunity to address open questions which lie beyond the capabilities of classical computations.

In this thesis we provide concrete protocols for quantum simulations of 2D effects in lattice gauge theories that can be performed with present-day technology. Our proposal overcomes the main challenges that are currently preventing us from accessing the rich phenomenology in gauge theories for particle physics beyond 1D and allows for proof-of-concept demonstrations of minimal instances in the lab. We consider quantum electrodynamics (QED), the gauge theory describing charged particles interacting through electromagnetic fields. Our approach allows for the simulation of the full theory, including dynamical matter and its interplay with gauge fields (see Ref. [17], for 2D proposals of pure gauge theories in 2D and Refs. [18, 19] for 2D proposals including dynamical matter that can be realized on future generations of quantum computers). In contrast to 1D QED which has no magnetic

field term, higher dimensions allow us to access magnetic field effects, while at the same time, the Fermi statistics of the matter fields become important. Unlocking those effects imposes various practical challenges, rendering quantum simulations beyond 1D inherently demanding. In particular, 1D QED allows for simplifications such as the elimination of the gauge field, resulting in a Hamiltonian description in terms of two-body terms only [8, 9, 20, 21]. This is in sharp contrast to higher spatial dimensions, where gauge fields cannot be eliminated and, as such, unavoidable many-body terms challenge possible implementations aimed at currently available quantum hardware. These difficulties for treating matter and gauge fields beyond 1D require novel approaches to render near-term demonstrations possible.

Here, we provide effective simulation techniques for simulating 2D lattice-QED systems with open and periodic boundary conditions. Our proposal entails two separate steps. In the first step, we formulate an effective Hamiltonian description using the techniques presented in Ref. [22] for simulating U(1) lattice gauge theories. We reduce the total Hilbert space to a small gauge-invariant subspace by eliminating redundant degrees of freedom. The original 2D-geometry of the theory is lost and we obtain an effective spin model. The second step consists of the implementation on quantum hardware. Our effective models from step 1 can in principle be simulated on a universal quantum computer. However, implementations in the current era of Noisy Intermediate-Scale Quantum (NISQ) technology [23] are challenging. In particular, resorting to analogue simulation approaches [12] is currently infeasible since engineering a simulator capable of performing the long-range many-body interactions required by our models has yet to be achieved. The appearance of many-body terms is inherent to 2D gauge theories, but hard to realize experimentally as current hardware is mostly based on short-range two-body interactions. The complexity of the interactions in our models arises from including both dynamical matter fields and a truncation of gauge fields beyond the minimal two-level description. Avoiding the often-used minimal two-level description of gauge fields dramatically increases the range of physical effects that can be captured by the model[1] and is needed to correctly approach the continuum limit [22].

In this thesis, we solve the problem of simulating these models with the limited resources provided by NISQ devices, by developing a hybrid quantum-classical Variational Quantum Eigensolver (VQE) algorithm [24] for current qubit-based quantum computers. We apply our so far general approach to the concrete case of trapped ion quantum computers,

---

[1]Approximating the gauge degrees of freedom as two-level systems leads for example to trivial electric field energy terms [see Sec. 2.1 and Eq. (2.2a)].

and provide a detailed experimental proposal for a minimal example that lies within the reach of quantum technologies available today [13, 25–27]. The protocols put forward in this work allow for exploring 2D effects in gauge theories for particle physics on quantum computers and bring this first experimental demonstration into reach.

We emphasize that using the new method put forward in Ref. [22] in our models provides us with the decisive tool to study 2D lattice gauge theories on lattices with arbitrary values of the lattice spacing a. In particular, our approach [22] reaches a well-controlled continuum limit $a \to 0$ while avoiding the problem of autocorrelations inherent to Markov Chain Monte Carlo (MCMC) methods. This offers the exciting long-term perspective to compute physical (i.e. continuum) quantities, such as bound state spectra, non-perturbative matrix elements, and form factors that can be related to collider and low energy experiments in the future. Studying these physical observables requires large lattices whose simulation is inaccessible to present-day quantum devices. However, various local quantities describe fundamental properties of a theory, and can be simulated on small lattices that are accessible today. An important simple example is the plaquette expectation value, as used in the pioneering work of Creutz [28] in the very beginning of MCMC simulations of lattice gauge theories. Despite its simplicity, the plaquette expectation value can be related to the renormalized running coupling that we consider below. Furthermore, the simulation methods presented here can be extended to models that include topological terms or finite fermionic chemical potentials and are therefore currently very hard or even inaccessible to MCMC due to the sign problem.

We treat the case of open boundary conditions within a ladder system (see Sec. 2.1). Although this system does not encompass the physics of the full 2D plane, it allows us to explore magnetic field properties on currently available quantum hardware. For that reason, we provide a simulation protocol for the basic building block of 2D lattice gauge theories, a single plaquette including matter, that demonstrates dynamically generated gauge fields. This is shown by observing the effect of particle-antiparticle pair creations on the magnetic field energy. In particular, we consider both positive and negative fermion masses. In the latter case, MCMC methods cannot be applied due to the zero mode problem [3, 4].

Additionally, we consider a single plaquette with periodic boundary conditions [see Fig. 2.2] to demonstrate that our approach provides an important first step towards calculating the so called "running coupling" in gauge theories [1, 2]. The running of the coupling, i.e. the dependence of the charge on the energy scale on which it is probed, is fundamental to gauge theories and is absent in 1D QED. The precise determination of the running cou-

pling, e.g. in quantum chromodynamics, is crucial to analyzing world-wide particle collider experiments. Here, we propose a first proof-of-concept quantum simulation of the running coupling for pure gauge QED.

In summary, we build on Ref. [22], which provides a method for casting gauge theories into effective spin models that are equipped with an efficient truncation scheme for the gauge fields. In this paper, we solve the problem of implementing these models on present-day quantum hardware. The paper is structured as follows. In Chap. 2, we introduce lattice QED and present the effective Hamiltonian description on which our proposal is based. We describe physical 2D phenomena that can be studied on small systems using our approach in Chap. 3. In the following Chap. 4, we show how to efficiently simulate these phenomena using hybrid quantum-classical simulations on qubit-based universal quantum computers. In Chap. 5, we focus on ion-based quantum computers. We explain why trapped ions are an excellent match for our approach in the NISQ era, and present a detailed experimental proposal, along with a classical simulation of the proposed experiments demonstrating that an implementation with present-day quantum computers is feasible. Finally, conclusions and outlooks are presented in Chap. 6.

Chapter 2

Simulated models

In this section, we introduce the models to be simulated in our proposal. In Sec. 2.1, we review the Hamiltonian formulation of lattice QED in $2 + 1$ dimensions along with the truncation applied to gauge degrees of freedom. The specific systems considered in the rest of this thesis are then described in Sec. 2.2 (open boundary conditions) and Sec. 2.3 (periodic boundary conditions).

2.1   Lattice QED in 2+1 dimensions

Although gauge theories are a fundamental component of the standard model, obtaining full analytical solutions is inherently challenging due to the number of Feynman diagrams which are required to obtain non-perturbative solutions. In fact, the best classical algorithm for determining the perturbative corrections to the dynamics at increasing energy scales exponentially. A successful tool for numerically investigating gauge theories is lattice gauge theory [1, 2], which involves the discretization of the Lagrangian or the Hamiltonian while preserving gauge symmetry. In the case of the former, one can perform MCMC-based methods, which have been very successful in investigating equilibrium properties. However, as mentioned in Chap. 1, MCMC methods are limited in certain parameter regimes by the sign problem [3, 4], which arises from the appearance of highly oscillatory terms (given rise to by the phases introduced by matter fields) in the integrals to be evaluated, therefore preventing efficient sampling from the distribution. Here, we aim to implement quantum simulation techniques, which circumvent these challenges, and are based on the Hamiltonian formulation of lattice gauge theory. Thus, we follow the approach pioneered by Kogut and Susskind in Ref. [29] to arrive at a Hamiltonian description of lattice QED

in 2D.

The Hamiltonian of Abelian and non-Abelian gauge theories in two (or more) dimensions is constructed in terms of electric and magnetic fields, and their coupling to charges. In continuous Abelian U(1) gauge theories like QED (and similarily for non-Abelian gauge theories like QCD), electric and magnetic fields are defined through the vector potential A_μ, with $E_\mu = \partial_t A_\mu$ and $B = \partial_x A_y - \partial_y A_x$ (in the unitary gauge). Here, t, x, y are the time and space coordinates in two dimensions, and $\mu = x, y$. Gauge invariance, i.e. invariance of the Hamiltonian under local phase (symmetry) transformations of the charges, follows directly from the invariance of E_μ and B under $A_\mu \to A_\mu + \partial_\mu \theta(x, y)$, where $\theta(x, y)$ is an arbitrary scalar function.

For lattice gauge theories in two dimensions, a square lattice is considered with charges defined on the vertices and gauge fields defined on the links. The electric interactions between charges at vertices i and j are described by the electric field operator $\hat{E}_{ij}$, which is Hermitian and possesses a discrete spectrum. Electric field operators take integer eigenvalues $e_{ij} = 0, \pm 1, \pm 2, \ldots$ with $\hat{E}_{ij}|e_{ij}\rangle = e_{ij}|e_{ij}\rangle$. The eigenstates $|e_{ij}\rangle$ form a basis for the gauge degrees of freedom.

For each link, one further defines a Wilson operator $\hat{U}_{ij}$, as the lowering operator for the electric field $[\hat{E}_{ij}, \hat{U}_{kl}] = -\delta_{i,k}\delta_{j,l}\hat{U}_{ij}$. The Wilson operator measures the phase proportional to the bare coupling g acquired by a unit charge moved along the link (i, j) of length a, i.e. $\hat{U}_{ij} \sim \exp[iag\hat{A}_\mu(i)]$. The magnetic interactions are given by (oriented) products of Wilson operators on the links around the plaquettes of the lattice.

Following the description given by Kogut and Susskind in Ref. [29], electrons and positrons are represented by single component fermionic field operators at each vertex. We use staggered fermions, meaning that odd (even)-numbered lattice sites i hold particles (antiparticles), as shown in Fig. 2.1(b). In other words, the fermionic raising operator $\hat{\psi}_i^\dagger$ creates (destroys) a particle (antiparticle) at odd (even) vertices, while the lowering operator $\hat{\psi}_i$ annihilates (creates) a particle (antiparticle) at odd (even) vertices [see Fig. 2.1(c)]. We refer to the vacuum as v, the particle as e, and the antiparticle as p. Using the convention of Fig. 2.1(b), we define the charge operator as

$$\hat{q}_i = Q\Big[\frac{\hat{\psi}_i^\dagger \hat{\psi}_i}{\|\hat{\psi}_i^\dagger \hat{\psi}_i\|_{\max}} - \frac{1}{2}\big(1 + (-1)^i\big)\Big], \qquad (2.1)$$

with eigenvalues $\{+Q, 0\}$ for odd lattice sites (presence or absence of particles) and $\{-Q, 0\}$ for even sites (presence or absence of antiparticles). We set $Q = 1$ in the remainder of this article [see Fig. 2.1(c)]. The factor $\|\hat{\psi}_i^\dagger \hat{\psi}_i\|_{\max} \equiv \max_{\psi_i} \langle \psi_i | \hat{\psi}_i^\dagger \hat{\psi}_i | \psi_i \rangle$ ensures proper normalization after a rescaling of the fermionic operators $\hat{\psi}_i$ (discussed later in this section).

Using this Kogut-Susskind formulation [29], we construct the Hamiltonian out of an electric, a magnetic, a mass, and a kinetic term; $\hat{H} = \hat{H}_{\mathrm{E}} + \hat{H}_{\mathrm{B}} + \hat{H}_{\mathrm{m}} + \hat{H}_{\mathrm{kin}}$, where

$$\hat{H}_{\mathrm{E}} = \frac{g^2}{2} \sum_{\substack{i \in \mathrm{sites}, \\ i \xrightarrow{+} j}} \hat{E}_{ij}^2, \tag{2.2a}$$

$$\hat{H}_{\mathrm{B}} = -\frac{1}{2g^2 a^2} \sum_{n=1}^{N} \left(\hat{P}_n + \hat{P}_n^\dagger \right), \tag{2.2b}$$

$$\hat{H}_{\mathrm{m}} = \frac{\widetilde{m}}{\alpha} \sum_{i \in \mathrm{sites}} (-1)^{i+1} \hat{\phi}_i^\dagger \hat{\phi}_i, \tag{2.2c}$$

$$\hat{H}_{\mathrm{kin}} = \frac{1}{2a\alpha} \left[\sum_{\substack{i \text{ odd}, \\ i \xrightarrow{+} j}} \hat{\phi}_i^\dagger \hat{U}_{ij} \hat{\phi}_j + \sum_{\substack{i \text{ even}, \\ i \xrightarrow{+} j}} \hat{\phi}_i \hat{U}_{ij}^\dagger \hat{\phi}_j^\dagger \right] + \mathrm{H.c.}. \tag{2.2d}$$

In the summations, we use $i \xrightarrow{+} j$ to denote the link between lattice sites i and j with positive orientation [see Fig. 2.1(a) and (b)], and n refers to plaquette n. We denote the bare coupling by g, $\widetilde{m}$ is the bare fermion mass, and a the lattice spacing. $\hat{\phi} = \hat{\psi}\sqrt{\alpha}$ is the rescaled field operator, with α being a dimensionless factor. We use here natural units $\hbar = c = 1$ and all operators in Eqs. (2.2) are dimensionless.

In the Hamiltonian above, we introduced the operator $\hat{P}_n = \hat{U}_{ij}^\dagger \hat{U}_{jk}^\dagger \hat{U}_{il} \hat{U}_{lk}$, where sites (i, j, k, l) form a closed loop clockwise around the plaquette n as in Fig. 2.1(b) [30]. This allows us to define the plaquette operator

$$\square = \frac{1}{2N} \sum_{n=1}^{N} \left(\hat{P}_n + \hat{P}_n^\dagger \right), \tag{2.3}$$

where N is the number of plaquettes.

At each vertex i, gauge invariance is imposed with the symmetry generators [18, 29] $\hat{G}_i = \hat{E}_{li} - \hat{E}_{ij} + \hat{E}_{ki} - \hat{E}_{im} - \hat{q}_i$ [see Fig. 2.1(d) for the definition of j, k, l, m]. Relevant, i.e. gauge-invariant quantum states are defined by Gauss' law $\hat{G}_i | \Psi_{\mathrm{phys}} \rangle = \epsilon_i | \Psi_{\mathrm{phys}} \rangle$
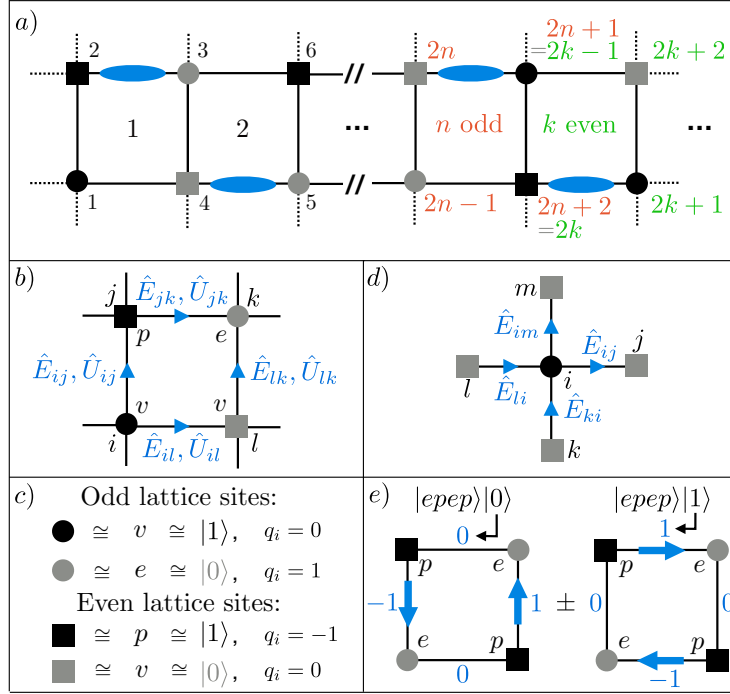
Figure 2.1: *Conventions for lattice QED in 2D. **(a)** Ladder system with open boundary conditions. Using Gauss' law, the number of gauge degrees of freedom can be reduced to one per plaquette (blue ellipses). **(b)** A single plaquette with matter sites at the vertices and gauge fields on the links. Circles (squares) represent odd (even) sites, and black (grey) corresponds to unoccupied (occupied) fermionic fields. Positive field direction is to the right and up. **(c)** Table showing the mapping between fermionic sites, particles (e), antiparticles (p), and vacuums (v), and spins. **(d)** Conventions for Gauss' law. **(e)** The two gauge-field configurations that minimize the electric field energy for a single plaquette with two particle-antiparticle pairs. As explained in the main text, these configurations are relevant for the 2D effects discussed in Sec. 3.1 (see App. C for more details).*

for each vertex of the lattice, where the eigenvalue ϵ_i corresponds to the background charge (static charges which can be arbitrarily added at each vertex) at site i. We consider the case $\epsilon_i = 0 \ \forall i$, but background charges can be easily included in the derivations below. In the continuum limit $a \to 0$ and three spatial dimensions, Gauss' law takes the familiar form $\nabla \hat{E} = \hat{\rho}$, where $\hat{\rho}$ is the charge density.

Gauge field operators are defined on infinite dimensional Hilbert spaces. To simulate them using finite-dimensional quantum systems, a truncation scheme is required. To implement a truncation taking $2l + 1$ basis states into account, we substitute the electric field operator

$\hat{E}$ and the lowering operator $\hat{U}$ with

$$\hat{E} \longmapsto \hat{S}^z, \tag{2.4a}$$

$$\hat{U} \longmapsto \hat{V}^-, \tag{2.4b}$$

where $\hat{S}^z$ is the z-component of a spin of length $|l| = \sqrt{l(l+1)}$. It is possible to define the operators $\hat{V}^-$ and $\hat{V}^+$ in several different ways, and we consider two main definitions. While both definitions are valid, each is advantageous in different applications. The first employs the spin lowering $\hat{S}^- = \hat{S}^x - i\hat{S}^y$ and raising $\hat{S}^+ = \hat{S}^x + i\hat{S}^y$ operators, such that $\hat{V}^- \equiv \hat{S}^-/|l|$ and $\hat{V}^+ \equiv \hat{S}^+/|l|$. The second prescribes

$$\hat{V}^- \equiv \begin{bmatrix} 0 & \dots & \dots & 0 \\ 1 & \dots & \dots & 0 \\ 0 & \ddots & \vdots & 0 \\ 0 & \dots & 1 & 0 \end{bmatrix}_{(2l+1)\times(2l+1)} \tag{2.5}$$

and $\hat{V}^+ = (\hat{V}^-)^\dagger$. Both definitions for $\hat{V}^-$ and $\hat{V}^+$ ensure that the commutation relations between $\hat{E}$ and $\hat{U}$ are recovered for $|l| \to \infty$. The specific choice of the truncation scheme depends on the quantum hardware that is employed. As an example, for quantum systems that allow for the implementation of interacting spin chains with large spins, such as $l = 1$ [31], the definition based on the spin lowering $\hat{S}^-$ and raising $\hat{S}^+$ is ideal. On the other hand, for qubit-based quantum hardware, it is convenient to employ Eq. (2.5). The encoding from spins to qubit is then simplified (see Sec. 4.1), and faster convergence to the full model is achieved. Switching from one definition to the other is trivial, with minor or no modifications in the Hamiltonians and the procedure. With the intention of implementing our model on an ion trap quantum computer as described in Chap. 5, we define the operators $\hat{V}^-$ and $\hat{V}^+$ according to Eq. (2.5) in the remainder of this thesis.

In the above, we established the conventions of Fig. 2.1 and arrived at the Hamiltonian for QED in 2D (Eqs. (2.2)). We identified a mapping to truncate the infinite dimensional gauge fields and represent them as an integer spin system. In the following section, we apply Gauss' law to achieve an effective Hamiltonian for a minimal instance of QED in 2D.

2.2 Effective Hamiltonian for open boundary conditions

In this section, we limit ourselves to considering a so-called ladder system (an array of plaquettes arranged in a horizontal line) with open boundary conditions [see Fig. 2.1(a)] rather than considering the entire 2D plane. Although this system does not encapsulate the full 2D physics of QED, it allows us to study important aspects of gauge theories that are not present in one spatial dimension, such as magnetic phenomena. In the following, we motivate and explain our approach to reduce the number of degrees of freedom by directly encoding Gauss' law into the Hamiltonian of the system. We then provide the effective Hamiltonian for the minimal instance of a single plaquette with a truncation of $l = 1$.

Universal quantum computers offer the possibility to perform gates between arbitrary pairs of qubits, i.e. the ability to implement long-range interactions. While most NISQ devices are capable of this, memory qubits are often scarce. This motivates our approach to minimize the number of degrees of freedom to be simulated (and hence the number of qubits needed) at the expense of introducing long-range interactions in our effective spin model.

More specifically, within the Hamiltonian formulations of a gauge theory, only a subsector of the whole Hilbert space consists of gauge-invariant states. In QED, this subspace is selected by applying Gauss' law with a specific choice of the static charges (see Sec. 2.1). As a result, it is possible to eliminate some of the gauge fields and obtain an effective Hamiltonian which is constrained to the specifically chosen subspace and operates on fewer qubits. This resource-efficient encoding results in long-range many-body interactions (as explained below). In Chaps. 4 and 5, we show how to efficiently implement these interactions using a VQE algorithm: a hybrid quantum-classical algorithm [24] which allows one to gain a quantum advantage using available experimental devices (explained in detail in Chap. 4).

The open boundary conditions for a ladder of N plaquettes appear as dashed lines in Fig. 2.1(a), indicating null background field. While there are $3N + 1$ gauge fields in the ladder, applying Gauss' law to all vertices reduces the independent gauge degrees of freedom to N. Given the freedom in choosing the independent gauge fields, we select the $(2n, 2n+1)$ links for each plaquette n, as shown by the blue ellipses in Fig. 2.1(a). On each link that does not hold an independent gauge field, the corresponding unitary operator $\hat{U}$ is set to the identity. As a result, the plaquette operator becomes $\hat{P}_n = \hat{U}_{2n,2n+1}$ and both the kinetic and magnetic terms are consequently simplified. To simulate this system

on qubit-based quantum hardware, we use the Jordan-Wigner transformation [32] to map fermions to spin-1/2 degrees of freedom, as shown in Fig. 2.1(c). The resulting effective Hamiltonian for the ladder is shown in App. A.

We now focus on the basic building block of the 2D ladder system, the plaquette [see Fig. 2.1(b)]. Setting $N = 1$ in Eqs. (A.1), the effective Hamiltonian for a single open boundary plaquette becomes

$$\hat{H}_{\mathrm{E}} = \frac{g^2}{2}\left[\left(\hat{S}_{23}^z\right)^2 + \left(\hat{S}_{23}^z + \hat{q}_2\right)^2 + \left(\hat{S}_{23}^z - \hat{q}_3\right)^2 + \left(\hat{S}_{23}^z + \hat{q}_1 + \hat{q}_2\right)^2\right], \tag{2.6a}$$

$$\hat{H}_{\mathrm{B}} = -\frac{1}{2g^2}\left(\hat{V}_{23}^- + \hat{V}_{23}^+\right), \tag{2.6b}$$

$$\hat{H}_{\mathrm{m}} = \frac{m}{2}\left(\hat{\sigma}_1^z - \hat{\sigma}_2^z + \hat{\sigma}_3^z - \hat{\sigma}_4^z\right), \tag{2.6c}$$

$$\hat{H}_{\mathrm{kin}} = -i\Omega\left(\hat{\sigma}_1^+\hat{\sigma}_2^- + \hat{\sigma}_1^+\hat{\sigma}_4^- - \hat{\sigma}_2^-\hat{V}_{23}^+\hat{\sigma}_3^+ + \hat{\sigma}_4^-\hat{\sigma}_3^+\right) + \mathrm{H.c.}, \tag{2.6d}$$

where $\hat{\sigma}_i^\pm = \frac{1}{2}(\hat{\sigma}_i^x \pm i\hat{\sigma}_i^y)$, and $\hat{\sigma}_i^x$, $\hat{\sigma}_i^y$, $\hat{\sigma}_i^z$ are the Pauli operators acting on the ith qubit, and we have used the mappings in Eqs. (2.4) and (2.5). We defined the rescaled fermion mass $m = \widetilde{m}/\alpha$, the strength of the kinetic term $\Omega = (2a\alpha)^{-1}$, and set the lattice spacing $a = 1$. Using the Jordan-Wigner transformation, the charge operator $\hat{q}_i$ becomes $\hat{q}_i = \frac{1}{2}\left(\hat{\sigma}_i^z - (-1)^i\right)$. The notation for describing the state of the plaquette is a tensor product of two kets, with the first ket representing the matter sites $1 - 4$ (v, e, and p are the vacuum, particle, and antiparticle, respectively) and the second ket the state of the gauge field on the $(2, 3)$ link [see Fig. 2.1(e)]. For example, the bare vacuum state is denoted as $|vvvv\rangle|0\rangle$.

In 1D QED, all gauge fields can be eliminated for systems with open boundary conditions. As a result, only two-body terms remain in the Hamiltonian [8, 9, 20, 21]. For the plaquette, many-body terms are unavoidable since gauge degrees of freedom remain. These additional terms increase the complexity in simulating the Hamiltonian significantly. However, the rich phenomenology (see Chap. 3) that becomes accessible motivate overcoming these challenges.

In the above, we have obtained a spin effective Hamiltonian for a single plaquette with open boundary conditions. Now, we do the same for a pure-gauge (i.e. no fermionic matter) plaquette with periodic boundary conditions, which allows us to study additional 2D phenomena.

11
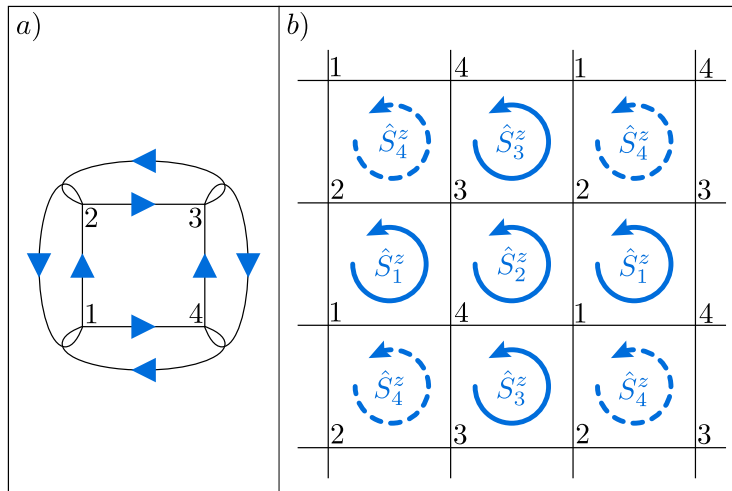
Figure 2.2: *Single periodic boundary plaquette for a pure gauge theory.* **(a)** *Representation in terms of the eight gauge fields (blue arrows), that are associated with the links of the lattice.* **(b)** *Representation in terms of independent gauge-invariant (i.e. physical) operators called "rotators". As explained in Ref. [22], the plaquette can be seen as an infinite lattice of plaquettes. Moreover, to explore ground state properties, only three independent rotators $\hat{S}_1^z$, $\hat{S}_2^z$, and $\hat{S}_3^z$ (shown in solid blue) are sufficient for describing the system.*

2.3 Effective Hamiltonian for periodic boundary conditions

In this section, we consider a square lattice with periodic boundary conditions. As explained in Sec. 2.2, we can use Gauss' law to eliminate a subset of gauge fields, resulting in an effective unconstrained Hamiltonian. In Ref. [22], we derive this effective Hamiltonian for lattice QED with periodic boundary conditions in full 2D, including dynamical fermionic matter. Here, we review Ref. [22] by summarizing the basic formulas and physical assumptions for the convenience of the reader.

The basic building block, a periodic boundary plaquette, includes eight gauge fields as shown in Fig. 2.2(a), and is equivalent to an infinite 2D lattice of four plaquettes [see Fig. 2.2(b)]. In the following, we consider the case of a single periodic boundary plaquette in the absence of matter, aiming at a proof-of-concept demonstration of a quantum simulation of the running coupling, i.e. the renormalization of the coupling constant for changing energy scales/lattice spacings (see Sec. 3.2). To this end, we consider the pure-gauge Hamiltonian $\hat{H}_{\mathrm{gauge}} = \hat{H}_{\mathrm{E}} + \hat{H}_{\mathrm{B}}$, given by Eqs. (2.2a) and (2.2b).

Since we are interested in studying ground state properties to demonstrate proof-of-concept 2D phenomena, it is sufficient to consider three independent gauge degrees of freedom [22], corresponding to the "rotators" $\hat{S}_i^z$, $i \in \{1, 2, 3\}$ shown in Fig. 2.2(b). While the system is fully characterized by five degrees of freedom, two in fact commute with the Hamiltonian and are thus constants of motion, and for studying ground state properties can be set to 0. Rotators are the natural choice for the gauge fields, as they represent the circulating electric field in a specific plaquette. As such, the operators $\hat{P}_n$ ($\hat{P}_n^\dagger$) in Eq. (2.3) are directly their annihilation (creation) operators.

For large values of the bare coupling g, the electric field term $\hat{H}_{\mathrm{E}}$ in $\hat{H}_{\mathrm{gauge}}$ is dominant and accordingly, the Hamiltonian representation with diagonal electric term described in Sec. 2.1 is efficient. For small g, however, the magnetic term $\hat{H}_{\mathrm{B}}$ is dominant, and the eigenstates of $\hat{H}_{\mathrm{gauge}}$ are superpositions of all electric field basis states. As such, any truncation scheme necessarily leads to large errors. To mitigate the truncation error, we apply the novel technique introduced in Ref. [22], which is briefly outlined below, and resort to two different formulations of the Hamiltonian. The electric formulation described in Sec. 2.2 is applied in the region $g^{-2} < 1$, while for $g^{-2} > 1$, a so-called magnetic basis is used, for which $\hat{H}_{\mathrm{B}}$ is diagonal. The process for obtaining the magnetic basis is somewhat more involved. Since the vector potential A_μ is a continuous degree of freedom (even on the lattice), it must be discretized and truncated. This is necessary to allow for an efficient description of the simulated ground state over sufficiently large values of the coupling g using only a limited number of basis states. We achieve this by using the cyclic group $\mathbb{Z}_{2L+1}$ ($L \in \mathbb{N}$) to approximate the continuous group $\mathrm{U}(1)$. The magnetic representation is obtained by first taking an approximation in the form of a series expansion that is exact for $L \to \infty$. We then apply the Fourier transform, and subsequently truncate the group $\mathbb{Z}_{2L+1}$ by only considering $l < L$ states in order to achieve equivalence to a truncated $\mathrm{U}(1)$ theory. As such, the basis becomes $|-l\rangle, ..., |0\rangle, ..., |l\rangle$. Here, L is the resolution of the discretization of the vector potential, and l represents the portion of the vector potential captured by the truncation. The relationship between L and l affects the ability of a truncation scheme to capture the spread of basis states around the magnetic basis ground state [22].

We thus arrive at the Hamiltonian $\hat{H}_{\mathrm{gauge}}^{(\gamma)} = \hat{H}_{\mathrm{E}}^{(\gamma)} + \hat{H}_{\mathrm{B}}^{(\gamma)}$, where $\gamma = e$ ($\gamma = b$) indicates

13

the electric (magnetic) representation, and

$$\hat{H}_{\mathrm{E}}^{(e)} = 2g^2\Big[(\hat{S}_1^z)^2 + (\hat{S}_2^z)^2 + (\hat{S}_3^z)^2 - \hat{S}_2^z(\hat{S}_1^z + \hat{S}_3^z)\Big], \tag{2.7a}$$

$$\hat{H}_{\mathrm{B}}^{(e)} = -\frac{1}{2g^2}\Big[\hat{V}_1^- + \hat{V}_2^- + \hat{V}_3^- + \hat{V}_1^-\hat{V}_2^-\hat{V}_3^- + \mathrm{H.c.}\Big], \tag{2.7b}$$

$$\hat{H}_{\mathrm{E}}^{(b)} = g^2 \sum_{\nu=1}^{2L} \Big\{ f_\nu^c \sum_{j=1}^{3} (\hat{V}_j^-)^\nu + \frac{f_\nu^s}{2}\big[(\hat{V}_2^-)^\nu - (\hat{V}_2^+)^\nu\big]$$

$$\times \sum_{\mu=1}^{2L} f_\mu^s\big[(\hat{V}_1^-)^\mu + (\hat{V}_3^-)^\mu\big] \Big\} + \mathrm{H.c.}, \tag{2.8a}$$

$$\hat{H}_{\mathrm{B}}^{(b)} = -\frac{1}{g^2}\Big\{ \sum_{i=1}^{3} \cos\Big[\frac{2\pi\hat{S}_i^z}{2L+1}\Big] + \cos\Big[\frac{2\pi(\hat{S}_1^z + \hat{S}_2^z + \hat{S}_3^z)}{2L+1}\Big] \Big\}. \tag{2.8b}$$

Here, $\hat{S}_i^z$, $\hat{V}_i^-$ and $\hat{V}_i^+$ are the operators defined in Sec. 2.1 associated with the ith rotator, in accordance with the truncation method explained in Sec. 2.1. Also,

$$f_\nu^s = \frac{(-1)^{\nu+1}}{2\pi}\Big[\psi_0\Big(\frac{2L+1+\nu}{2(2L+1)}\Big) - \psi_0\Big(\frac{\nu}{2(2L+1)}\Big)\Big], \tag{2.9}$$

$$f_\nu^c = \frac{(-1)^\nu}{4\pi^2}\Big[\psi_1\Big(\frac{\nu}{2(2L+1)}\Big) - \psi_1\Big(\frac{2L+1+\nu}{2(2L+1)}\Big)\Big], \tag{2.10}$$

where $\psi_k(\cdot)$ is the k-th polygamma function [22]. We note that making use of electric and magnetic representations in the case of the open boundary plaquette (see Sec. 2.2) can be done in the same way. However, we use this formulation only for the periodic boundary plaquette.

14

Chapter 3

Quantum simulation of 2D effects

In this section, we use the effective Hamiltonian description and truncation scheme provided in Chap. 2 to study phenomena in lattice QED with open boundary conditions (Sec. 3.1) and periodic boundary conditions (Sec. 3.2). While next generation quantum computers will widen the scope of our approach, we focus here on phenomena that can be studied with small system sizes and for which quantum simulations can be carried out on current quantum hardware. Detailed experimental protocols for realizing the quantum simulations proposed in this section using an ion-based quantum computer will be given in Sec. 5.

3.1 Dynamical matter and magnetic fields

We describe a minimal example that allows for the study of 2D effects in lattice QED with open boundary conditions. More specifically, we examine the appearance of dynamically generated magnetic fields due to particle-antiparticle creation processes within a single plaquette. This effect manifests itself in an abrupt switch of the ground state, resulting from the competition between the kinetic and magnetic terms in the QED Hamiltonian of Eqs. (2.6). There are two parameter regimes in which this phenomenon occurs. In one, the parameter Ω [see Eq. (2.6d)] is dominant if compared to the mass and the bare coupling g, allowing the kinetic and the magnetic terms to be the leading contributions to the energy. Alternatively, the transition of the ground state appears when the mass is smaller than zero (or with positive mass and non-zero background field). This last scenario is hard to simulate using MCMC methods, in which the use of the inverse of the lattice Dirac operator in combination with a negative mass induces zero modes [33], leading to unstable simulations. We note that in 1D QED, considering a negative fermion mass is equivalent

to a theory with positive mass in the presence of a topological term $\theta = \pi$ (see e.g. [34])[1]. It will be interesting to investigate the relation of the negative fermion mass to a theory in the presence of a topological term in $2+1$ dimensions.

The proposed experiment consists of preparing the ground states of Eqs. (2.6) for different values of the coupling g, and subsequently measuring the magnetic field energy, which is proportional to $\langle \square \rangle$ [see Eq. (2.3)]. In the strong coupling regime $g^{-2} \ll 1$, the magnetic field energy vanishes $\langle \square \rangle = 0$, since the ground state approaches the bare vacuum $|vvvv\rangle|0\rangle$. For weak couplings, $g^{-2} \gg 1$, the magnetic term dominates and the ground state is a superposition of all electric field basis elements. As such, $\langle \square \rangle$ converges to 1 when $g^{-2} \to \infty$. However, the truncation described in Sec. 2.1 bounds $\langle \square \rangle$ to a smaller value [22].

To explain the underlying physics in the intermediate region between the strong and weak coupling regimes, we first examine the case in which the kinetic term of the Hamiltonian can be treated as a perturbation (Fig. 3.1). Perturbative calculations are valid for $1 \ll \Omega \ll |4m|$, and we show results for $\Omega = 5$ and $m = -50$. We then proceed to the non-perturbative case (Fig. 3.2) with parameters $\Omega = 5$ and $m = 0.1$. Our analytical results within the perturbative regime are determined using our iterative algorithm described in App. B.

For $\Omega = 5$ and $m = -50$, the kinetic term can be treated as a perturbation, and we take the sum of the electric and mass terms in Eqs. (2.6a) and (2.6c) as the bare Hamiltonian. We can thus well describe the strong coupling regime $g^{-2} \ll 1$, in which a 2D effect occurs that is characterized by a jump of the expectation value of the plaquette operator. A plot of $\langle \square \rangle$ as a function of g^{-2} is shown in Fig. 3.1(a), where the black dashed line is obtained using exact diagonalization of the Hamiltonian in Eqs. (2.6) for a truncation $|l| = 1$, and the coloured lines correspond to perturbative calculations. We begin by analyzing the system for $g^{-2} \ll 1$ (marked as region 1 in Fig. 3.1), and examine increasing values of g^{-2} as we move through regions 2 and 3.

In region 1, the ground state of the Hamiltonian is the bare vacuum $|vvvv\rangle|0\rangle$, which is characterized by null energy and $\langle \square \rangle = 0$. The dominating electric term prevents the creation of electric field, despite the mass term incentivizing particle-antiparticle pair cre-

---

[1]In principle, the fermion mass can be written with a phase factor $m_e^{i\theta}$. In 1D QED, the anomaly equation (see the appendix of Ref. [34]) can be used to eliminate this phase by a rotation, and it appears as the topological term in the gauge field. This means that by working with a negative fermion mass, the model is equivalent to a theory with a θ term at $\theta = \pi$.

ation ($m < 0$). The magnetic term is negligible in the strong coupling regime. With increasing g^{-2}, the cost of creating electric fields is reduced, until it becomes favourable to create particle-antiparticle pairs. In particular, for $g^{-2} = -(4m)^{-1}$, the energy relief $2m$ of creating a pair compensates the cost $g^2/2$ of creating an electric field on the link connecting the pair.

The kinetic term $\hat{H}_{\mathrm{kin}}$ is responsible for the energy anti-crossing between regions 1 and 2 as it allows the creation of particle-antiparticle pairs and the corresponding electric fields. It allows the ground state to transition from the vacuum to a plaquette state which contains the maximum number of particle-antiparticle pairs (we refer to this as a fully-filled plaquette). However, Gauss' law allows two different gauge field configurations for the fully-filled plaquette, as shown in Fig. 2.1(e). These states are given by $|f_{\pm}^{(0)}\rangle = \frac{1}{\sqrt{2}}|epep\rangle(|0\rangle \pm |1\rangle)$, and while they are degenerate with respect to the bare Hamiltonian $\hat{H}_{\mathrm{E}} + \hat{H}_{\mathrm{m}}$, $\langle\hat{H}_{\mathrm{kin}}\rangle$ is minimized for $|f_-\rangle$ and $\langle\hat{H}_{\mathrm{B}}\rangle$ for $|f_+\rangle$. The existence of these two configurations in the presence of the perturbation $\hat{H}_{\mathrm{kin}}$ and the magnetic term $\hat{H}_{\mathrm{B}}$ creates competition between two quasi-degenerate vacua in regions 2 and 3 of Fig. 3.1(b). The ground states in these regions are described by the corresponding corrected states in perturbation theory $|f_{\pm}\rangle = \sum_n |f_{\pm}^{(n)}\rangle$ (see App. B), as shown in Fig. 3.1(b). Here, we see that the kinetic term facilitates the creation of particle-antiparticle pairs and drives the ground state from the vacuum in region 1 towards $|f_-\rangle$ in region 2.

The remarkable 2D feature of the theory is the jump of $\langle\square\rangle$ between regions 2 and 3, which is shown by the black dotted line in Fig. 3.1(a). This jump corresponds to the sharp energy anti-crossing in Fig. 3.1(b), and follows from the competition between the quasi-degenerate vacua in the presence of the kinetic and magnetic terms. As the relative weights of $\hat{H}_{\mathrm{kin}}$ and $\hat{H}_{\mathrm{B}}$ change with g^{-2}, an anti-crossing occurs and the ground state changes from $|f_-\rangle$ to $|f_+\rangle$. More specifically, there is a value g_{c} such that, for any $g^{-2} > g_{\mathrm{c}}^{-2}$, $E_{\mathrm{B}}^{(+)} + E_{\mathrm{kin}}^{(+)} < E_{\mathrm{B}}^{(-)} + E_{\mathrm{kin}}^{(-)}$, where $E_{\alpha}^{(\pm)} = \langle f_{\pm}|\hat{H}_{\alpha}|f_{\pm}\rangle$. Despite the fact that the magnetic Hamiltonian is not included in our perturbative analysis, we can analytically calculate this value g_{c} (see App. B). By requiring the magnetic and kinetic contributions from the energy to be equal, we find $g_{\mathrm{c}} = 0.012 + o(\Omega^8)$, which is in excellent agreement with the results obtained from exact diagonalization [see Fig. 3.1(a)]. Following the jump, in region 3, the ground state is thus $|f_+\rangle$, until we reach the weak coupling regime and the magnetic term becomes dominant compared to all other contributions.

The analysis above shows how pair creation processes can lead to dynamically generated magnetic fluxes that result in negative values of the magnetic field energy. For negative

17

mass, the considered effect of competing vacua occurs over a wide range of parameters. The strength of the kinetic term Ω broadens the dip and shifts the position of the jump g_c.

In the following, we consider the regime in which the kinetic term cannot be treated as a perturbation. For $\Omega = 5$ and $m = 0.1$, exact diagonalization results are shown in Fig. 3.2(a). In the intermediate region where $g \simeq 1$, the kinetic term has significant weight, which leads to entanglement between matter and gauge degrees of freedom in the ground state. In particular, in the limit $\Omega \gg |m|, g^2, g^{-2}$ and for $l \to \infty$, it can be shown for N plaquettes [35] that the energy is minimized for a magnetic flux of π, which is generated by pair creation processes and corresponds to $\langle \square \rangle = -1$ (which is not reached in Fig. 3.2(a) due to the effects of truncation). Figs. 3.2(b)-(d) show the probabilities of the components of the ground state at different values of g^{-2}. In the strong and weak coupling regimes, the ground states are the vacuum $|vvvv\rangle|\mathrm{GS}^{(e)}\rangle$ and $\frac{1}{2}(|vvvv\rangle-|epep\rangle+i|epvv\rangle+i|vvep\rangle)|\mathrm{GS}^{(b)}\rangle$, respectively, where $|\mathrm{GS}^{(e)}\rangle = |0\rangle$ is the gauge component of the ground state of the electric term and $|\mathrm{GS}^{(b)}\rangle$ is that of the magnetic term (see App. C). For $g^{-2} = 1$, however, the ground state approximates the ground state of the truncated kinetic term for $l = 1$ with 92% fidelity (which can be increased by incrementing Ω). To quantify the ground state entanglement between matter and gauge degrees of freedom, we calculate the entanglement entropy $\mathcal{S}(\rho_g) = -\mathrm{Tr}[\rho_g \log \rho_g]$, where ρ_g is the density matrix of the gauge subsystem. The entanglement entropy is plotted as the red dashed line in Fig. 3.2(a) and shows that the matter and gauge subsystems are entangled over a wide range of parameters.

3.2   Running coupling

In this section, we consider 2D effects in QED on a lattice subject to periodic boundary conditions. The method described in Sec. 2.3 and in Ref. [22] is based on the Hamiltonian formalism of lattice gauge theories, which allows for simulations that are unaffected by the problem of autocorrelations inherent to MCMC methods. Thus, we can compute physical observables at arbitrary values of the lattice spacing, ultimately allowing for reaching a well-controlled continuum limit. As such, quantum hardware could be used to efficiently calculate, for instance, the bound state mass spectrum of the theory, properties of the inner structure of such bound states, or form factors which are important for experiments [1, 33]. However, such quantities require computational capabilities which are not accessible on present quantum devices.

We are therefore bound to consider local observables which only need a small number of lattice points. We consider the plaquette operator $\Box$ as a simple example, as was done in the pioneering work by Creutz [28] in the beginning of MCMC simulations of lattice gauge theories. Despite its local nature, the operator $\Box$ can be related to a fundamental parameter of the theory, namely the renormalized coupling g_{ren} [36]. Importantly, the 1D Schwinger model is super-renormalizable, meaning that the coupling does not get renormalized, while, as we will show, renormalization is necessary for our 2D model. Thus, the 2D model investigated here represents an important step forward for lattice (quantum) simulations based on the Hamiltonian formalism.

Renormalization appears in quantum field theories through quantum fluctuations, i.e. the spontaneous generation of particle-antiparticle pairs from the vacuum. This phenomenon leads to a charge shielding (or anti-shielding for non-Abelian gauge theories) [37], which in turn changes the strength of the charge depending on the distance (or the energy scale) at which it is probed. As such, the charge becomes *scale dependent* and in this work we choose the inverse lattice spacing $1/a$ as the scale. The scale dependence, which is a renormalization effect, is referred to as the *running* of the coupling and its knowledge is fundamental in understanding the interactions between elementary particles. In particular, the running coupling serves as an input to interpret results from collider experiments, such as the Large Hadron Collider. Hence, the ability to compute the running coupling from the plaquette operator can have a direct impact on such experiments and our knowledge of elementary particle interactions.

As explained in Sec. 2.3, we study the case of two-dimensional QED without matter. Despite the absence of matter, and in contrast to the previously studied 1D Schwinger model, renormalization is needed, and hence the calculation of the running coupling. A definition of the renormalized coupling g_{ren} can be given through the ground state expectation value of the plaquette $\langle\Box\rangle$ [36]

$$g_{\mathrm{ren}}^2 = \frac{g^2}{\langle\Box\rangle^{1/4}}, \tag{3.1}$$

where g is the bare coupling from the Hamiltonian [see Eqs. (2.7) and (2.8)]. By looking at Eq. (3.1), it follows that to cover the scale dependence of the coupling, we need to evaluate $\langle\Box\rangle$ over a broad range of the lattice spacing a. Equivalently (we set $a = 1$ above), this means that we need to perform simulations at many values of g^{-2}, covering the whole spectrum between the extremal regions of strong and weak couplings, $g^{-2} \ll 1$ and $g^{-2} \gg 1$, respectively. In particular, the interesting region where perturbation theory is no longer applicable and bound states can be computed on not too large lattices is where

$g^{-2} \simeq 1$. Covering such a broad range of scales is the major problem in standard lattice gauge simulations. In fact, while approaching the weak coupling regime, autocorrelation effects prevent calculations from reaching very small values of the lattice spacing, making continuum extrapolations and hence convergence to meaningful results difficult. We remark that in large scale lattice simulations, much more sophisticated definitions of the renormalized coupling g_{ren} are generally used [1, 38]. These alternative definitions allow, besides other things, to disentangle cut-off effects, inherent to the plaquette coupling, from the true physical running. However, the alternative forms of g_{ren} described in [1, 38] are meaningful for large lattices only, and are hence beyond the capabilities of current quantum simulators. In this work, we allow for a proof-of-concept demonstration which paves the way to future improvements.

With our method (see Sec. 2.3 and Ref. [22]), we can simulate the system both in the strong and in the weak coupling regimes, with very modest truncations. The most difficult region to simulate is characterized by $g^{-2} \simeq 1$, where convergence is studied in Ref. [22]. We demonstrate this in Fig. 3.3, where the ground state expectation value of the plaquette operator $\langle \Box \rangle$ is plotted against g^{-2}. For periodic boundary conditions, the plaquette operator is given by $\Box = -\frac{g^2}{4} \hat{H}_{\mathrm{B}}^{(\gamma)}$ where $\gamma = e$ ($\gamma = b$) refers to the electric (magnetic) representation [see Eqs. (2.7b) and (2.8b)]. Accordingly, the blue and red lines are determined with these two representations, while the black, dotted lines are obtained using perturbation theory, and describe well the exact results in the extremal regions. The left graph is for a truncation $l = 1$ and the right for $l = 2$.

As shown in Ref. [22], the electric representation accurately describes the model in the weak coupling regime $g^{-2} \ll 1$ while the magnetic one in the other extremum $g^{-2} \gg 1$. Increasing the truncation from $l = 1$ to $l = 2$ for intermediate bare coupling values $g \simeq 1$ leads to great improvement in the middle region of the plot in Fig. 3.3(a). In fact, for increasing l, the two representations are more consistent in the intermediate coupling regime. As proven in Ref. [22], the smaller this minimum distance is, the better is the convergence to the U(1) result, for any value of the bare coupling g^{-2}. In particular, by switching from the electric representation at small couplings to the magnetic one in this intermediate region, it is possible to smoothly connect the weak and strong coupling regimes. In other words, we cover the whole range of the corresponding lattice spacings, or, equivalently, the scales $1/a$.

In Chap. 5, we provide a protocol for simulating the system with a truncation $l = 1$ of the gauge field using 9 qubits. As shown in Fig. 3.3, using a truncation $l = 2$ around the region of the plot where $g^{-2} \simeq 1$ brings us much closer to the converged result. Using

the same protocol as for $l = 1$ (see Chap. 4), the simulation for $l = 2$ requires 15 qubits.
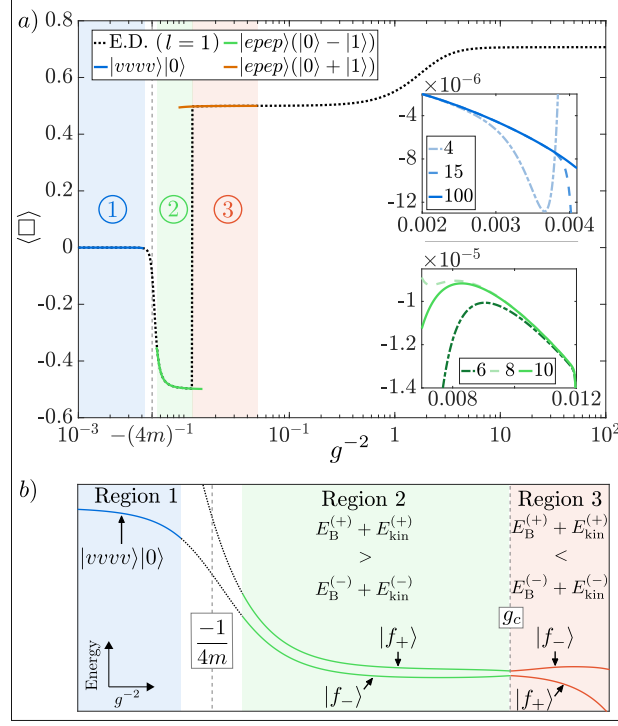
Figure 3.1: **(a)** *Plaquette expectation value as a function of g^{-2} for a single plaquette with mass $m = -50$ and kinetic strength $\Omega = 5$. Regions 1, 2, and 3 correspond to the numbered regions in part (b) below. Exact diagonalization of the truncated model is represented by the black dashed line, and perturbation theory was used for the blue, green, and orange lines. The insets are magnifications of parts of regions 1 and 2 (blue and green, respectively), plotting the difference between exact diagonalization and perturbation theory of order reported in the legend to confirm convergence to the full U(1) theory. The difference is not completely vanishing due to the small contribution of the magnetic term which is ignored in perturbative calculations.* **(b)** *Schematic representation of the ground and first excited state's energy, which illustrates the transition of the ground state due to competition between the kinetic and magnetic terms in the Hamiltonian.*
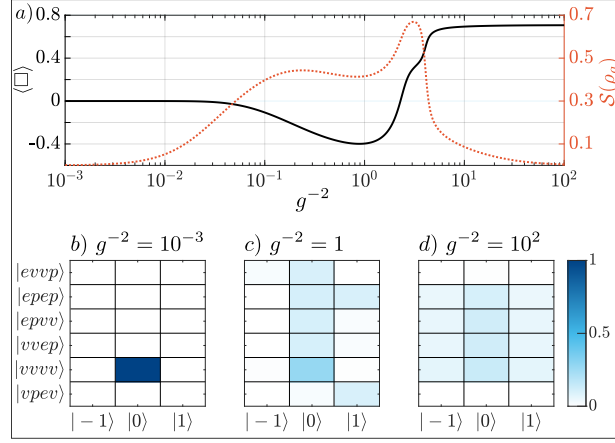
Figure 3.2: *Ground state properties in the non-perturbative regime.* **(a)** *Plaquette operator expectation value ⟨□⟩ and entanglement entropy $\mathcal{S}(\rho_g)$ as a function of g^{-2}.* **(b)-(d)** *The probability by component of the ground state for the indicated g^{-2}. At $g^{-2} = 10^{-3}$, the lowest energy state is the vacuum $|vvvv\rangle|0\rangle$. For $g^{-2} = 1$, the ground state approximates that of the kinetic term. For large g^{-2}, the magnetic Hamiltonian in the presence of the kinetic Hamiltonian yields the tensor product between a superposition of matter states and the gauge ground state of the magnetic term. Through (a) - (d), we used $\Omega = 5$ and $m = 0.1$, and a gauge field truncation $l = 1$.*
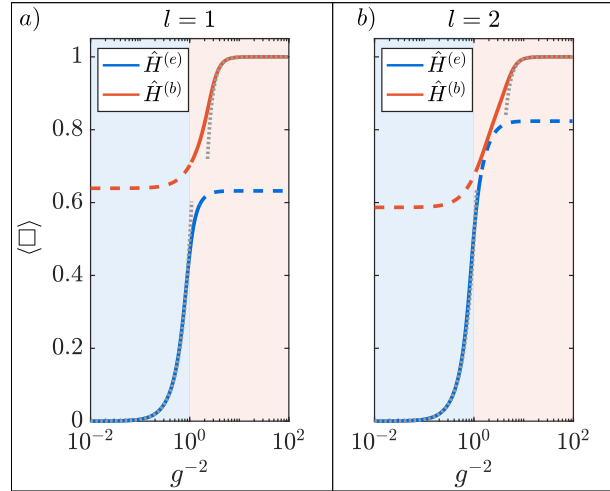
Figure 3.3: *Ground state expectation value of the plaquette operator □ for a pure gauge periodic boundary plaquette (see Fig. 2.2). Results obtained using the electric and magnetic representation are shown as blue and red lines, respectively. Perturbative calculations are shown as black dashed lines. The plots correspond to two different truncations $l = 1$ and $l = 2$, as indicated above. The blue (red) shaded region indicates the values of g^{-2} for which the the electric (magnetic) representation achieves the best results.*

23

Chapter 4

Qubit encoding and variational quantum eigensolver

In the previous sections, we presented an effective Hamiltonian description along with 2D phenomena to be studied. In the following, we explain the software protocols for simulating our models on quantum hardware. Assuming a universal qubit-based quantum computer, in Sec. 4.1 we provide an efficient encoding of the gauge fields in terms of qubits. Since currently available quantum computers have limited system size and number of gates, it is advantageous to employ a variational quantum eigensolver (VQE) approach, as explained in Sec. 4.2. To facilitate a VQE of the complicated models described in Secs. 3.1 and 3.2, in Sec. 4.3 we present an efficient measurement scheme suitable for any qubit-based quantum device. This scheme reduces the experimental requirements for implementation by efficiently grouping commuting observables. Concrete VQE circuits will be discussed in Chap. 5. For NISQ hardware, the question of optimal circuit design becomes platform-specific, and we will provide a detailed experimental proposal for trapped ions.

4.1 Qubit encoding

To simulate QED beyond 1D on qubit-based quantum devices, gauge fields need to be encoded into qubits. We truncated the infinite dimensional gauge degrees of freedom according to Eqs. (2.4) and (2.5), and here we describe how the resulting truncated models [see Eqs. (2.6), (2.7), and (2.8)] can be efficiently mapped to a sector of an appropriate qubit Hilbert space. We remark that our qubit encoding scheme is not unique, but practical for the proposed quantum simulation experiments, as we explain below.

For a given l, each gauge degree of freedom is described by the $2l + 1$ states $|e\rangle$, $e = -l$, $-l + 1, \ldots, 0, \ldots, l - 1, l$. We map this vector space onto $2l + 1$ qubits using the mapping

$$| - l + j\rangle = |\overbrace{0\ldots0}^{j}1\overbrace{0\ldots0}^{2l-j}\rangle, \tag{4.1}$$

where $0 \leq j \leq 2l$. With this encoding, the gauge field operators take the simple form

$$\hat{S}^z = \frac{1}{2}\sum_{i=1}^{2l}\prod_{j=1}^{i}\hat{\sigma}_j^z, \tag{4.2a}$$

$$\hat{V}^- = \sum_{i=1}^{2l}\hat{\sigma}_i^-\hat{\sigma}_{i+1}^+, \tag{4.2b}$$

and we recover the relations $\hat{S}^z|e\rangle = e|e\rangle$ and $\hat{V}^-|e\rangle = (1 - \delta_{e,-l})|e - 1\rangle$ for all $-l \leq e \leq l$.

Since this encoding only uses a subsector of the $2l + 1$ qubits' Hilbert space, the VQE should avoid gauge field qubit states that are not of the form given in Eq. (4.1). To this end, several strategies can be employed. For example, the VQE circuit (see Secs. 4.2, 5.2 and 5.3) can be constructed using a gate set that preserves the total spin $\hat{S}_{tot}^z = \sum_n \hat{\sigma}_n^z$ for each gauge field. Starting from an initial state with the correct total spin guarantees that the quantum computer only accesses states that are within the physical subspace identified by Eq. (4.1). Note that by using Eq. (4.1) for the encoding of the gauge fields, the resulting Hamiltonians (including matter fields) preserve the total magnetization, which is advantageous for trapped ion implementations (see Sec. 5.1). We use this solution in our circuit design in Chap. 5. Alternatively, different strategies can be employed, such as the addition of an energy penalty term to the Hamiltonian, which makes it energetically unfavourable for the system to leave the physical subspace. We remark, however, that altering the energy landscape of the model can affect the performance of the VQE.

4.2 Hybrid quantum-classical simulation

Applying the qubit encoding from Sec. 4.1 to the effective gauge-invariant description of our target models provided in Chap. 2 yields complicated Hamiltonians. These involve exotic long-range interactions and many-body terms that are beyond the capabilities of current

analogue quantum simulations. Resorting to digital approaches, one could in principle perform a Trotterized adiabatic state preparation [39]. However, due to the complexity of our models, this approach is also infeasible for the technology available today. In the absence of large-size high-precision quantum computers, we therefore choose a hybrid quantum-classical strategy, using a VQE protocol that brings the observation of the effects described in Chap. 3 within reach of present-day quantum devices. In fact, VQE protocols are already successfully used in quantum chemistry [24, 40–42], nuclear physics [43, 44] and classical applications [45].

A VQE is an iterative procedure in which a quantum device is connected in a closed feedback loop with an optimization algorithm performed by a classical computer [13, 24, 46]. The quantum device is interrogated by measuring a given cost function $\mathcal{C}(\boldsymbol{\theta})$ for a parameterized variational state $|\Psi(\boldsymbol{\theta})\rangle = U(\boldsymbol{\theta})|\Psi_{\text{in}}\rangle$. Here, $|\Psi_{\text{in}}\rangle$ is an initial state that can be easily prepared, and $U(\boldsymbol{\theta})$ is the application of a quantum circuit involving variational parameters $\boldsymbol{\theta}$. The classical optimization algorithm minimizes $\mathcal{C}(\boldsymbol{\theta})$ by querying the quantum device (see Sec. 5.4). Since our quantum simulations aim at preparing the system's ground state (see Chap. 3), our VQE cost function is given by the expectation value of the target Hamiltonian in the variational state, $\mathcal{C}(\boldsymbol{\theta}) = \langle\Psi(\boldsymbol{\theta})|\hat{H}_T|\Psi(\boldsymbol{\theta})\rangle$. In each iteration of the feedback loop, the classical optimizer provides updated variational parameters to minimize $\mathcal{C}(\boldsymbol{\theta})$.

Importantly, the target Hamiltonian is not physically realized on the quantum hardware. Instead, its expectation value can be estimated from a series of measurements of the variational state [24, 42] (see Sec. 4.3). This approach is usually insensitive to systematic errors, and both relaxes the quantum resource requirements and allows for ground state calculations of complex models, as we will show in the remainder of this paper.

4.3   Hamiltonian averaging

Our VQE algorithm requires the measurement of the energy of the variational state, i.e. the cost function $\mathcal{C}(\boldsymbol{\theta})$. Precise estimation of the expectation value of a complicated Hamiltonian demands, in general, a large number of measurements, which translates to extensive computational runtime. In this section, we show how the number of measurements required for the proposed quantum simulations can be substantially reduced by combining the standard approach [24, 42] with the measurement strategy put forward in Ref. [47]. As

explained in the following, we adapt the latter to our models and provide circuits for their implementation on different types of quantum hardware. The described scheme assumes local measurements only.

By using Pauli operators as a basis, we can express any target Hamiltonian $\hat{H}_T$ as

$$\hat{H}_T = \sum_{k=1}^{K} c_k \hat{Q}_k, \tag{4.3a}$$

$$\hat{Q}_k = \bigotimes_{i=1}^{n} \hat{\sigma}_i^{k_i}, \tag{4.3b}$$

where K is the number of terms in the decomposition, n is the dimension of the system, $\hat{\sigma}_i^{k_i}$ is a Pauli operator acting on the ith qubit and k_i can either be 0 (identity), x, y, or z for any i. We remark that, for our qubit encoding (see Sec. 4.1), decomposing the Hamiltonian as in Eq. (4.3a) can be efficiently done using the relations given in Eq. (4.2).

The cost function $\mathcal{C}(\boldsymbol{\theta})$ is evaluated by measuring the expectation values $\langle \hat{Q}_k \rangle$ with single-qubit Pauli measurements and calculating the weighted sum $\langle \hat{H}_T \rangle = \sum_{k=1}^{K} c_k \langle \hat{Q}_k \rangle$. Operators $\hat{Q}_k$ that commute with each other can be measured simultaneously and will be grouped together in the following. Thus, we rewrite Eq. (4.3a) as $\hat{H}_T = \sum_{m=1}^{M} \hat{R}_m$, where

$$\hat{R}_m = \sum_{k \in \mathcal{V}_m} c_k \hat{Q}_k. \tag{4.4}$$

Here, the set $\mathcal{V}_m$ contains indices of commuting operators $\hat{Q}_k$. Importantly, the number M of commuting sets can be drastically smaller than the total number of Pauli operators K in Eq. (4.3a), leading to a reduction in the experimental runtime.

To successfully run a VQE algorithm, we must be able to calculate the average values of the energy for any variational state preparation. Due to the statistical nature of quantum mechanics, the exact average value of any observable is unknown. Thus, we need to approximate the energy with an estimator. For a generic operator $\hat{O}$, we denote the estimator of its expectation value $\langle \hat{O} \rangle$ with $\bar{O}$. Depending on the intrinsic variance $(\Delta \hat{O})^2$ and the number of repeated measurements performed, the estimator $\bar{O}$ is affected by a statistical error, which is characterized by its variance $\text{Var}[\bar{O}]$.

To approximate the system's energy, we choose beforehand a certain precision, which is generally problem and/or application dependent. In practice, this means that we are required

to fix a threshold ϵ^2, and repeat energy measurements $\bar{H}_T$ until its variance $\mathrm{Var}[\bar{H}_T]$ becomes smaller than ϵ^2. Since $\hat{H}_T$ is the sum of the independent operators $\hat{R}_m$ [see Eq. (4.4)], $\bar{H}_T$ can be expressed in terms of the estimators for the $\langle \hat{R}_m \rangle$ as $\bar{H}_T = \sum_{m=1}^{M} \bar{R}_m$. More specifically, each estimator $\bar{R}_m$ is found by averaging N_m measurement outcomes $\{r_m^i\}$, i.e.

$$\bar{R}_m = \frac{1}{N_m} \sum_{i=1}^{N_m} r_m^i. \tag{4.5}$$

For sufficiently large N_m, the variance of the estimators $\bar{R}_m$ is $\mathrm{Var}[\bar{R}_m] \simeq (\Delta \hat{R}_m)^2 / N_m$, where $(\Delta \hat{R}_m)^2$ is the intrinsic variance of the operator $\hat{R}_m$ with respect to the considered state. Since the operators $\hat{R}_m$ are measured in different experimental runs, the estimators $\bar{R}_m$ are independent and thus have zero covariance $\mathrm{Cov}[\bar{R}_i, \bar{R}_j] = 0$. As such, we can express $\mathrm{Var}[\bar{H}_T]$ as the sum

$$\mathrm{Var}[\bar{H}_T] = \sum_{m=1}^{M} \mathrm{Var}[\bar{R}_m]. \tag{4.6}$$

Achieving an error in $\bar{H}_T$ of no more than ϵ requires $\mathrm{Var}[\bar{H}_T] = \epsilon^2$. Assuming equal contribution from each of the $\bar{R}_m$, we write $\mathrm{Var}[\bar{R}_m] = \epsilon^2/M$. Substituting $\mathrm{Var}[\bar{R}_m] \simeq (\Delta \hat{R}_m)^2 / N_m$, the number of measurements for each m is $N_m \simeq M(\Delta \hat{R}_m)^2 / \epsilon^2$, and, summing over m, the total number of measurements N is

$$N \simeq \frac{M}{\epsilon^2} \sum_{m=1}^{M} (\Delta \hat{R}_m)^2. \tag{4.7}$$

Besides the chosen threshold ϵ^2, the total number of measurements N is proportional to the intrinsic variances $(\Delta \hat{R}_m)^2$ and the number of partitioned sets M. In general, there are many different ways to partition the $\hat{Q}_k$ into the $\hat{R}_m$, and we seek to identify a strategy which minimizes both M and $(\Delta \hat{R}_m)^2$. Importantly, $(\Delta \hat{R}_m)^2$ depends on the intrinsic variances and the covariances of the $\hat{Q}_k$ from which each $\hat{R}_m$ is comprised. While a particular partitioning strategy might achieve $M < K$, it might also group together $\hat{Q}_k$ with positive covariance, thereby adding to $(\Delta \hat{R}_m)^2$ and increasing the number of measurements needed to achieve ϵ^2 precision of $\bar{H}_T$. For instance, as pointed out in Ref. [24], the Hamiltonian

$$\hat{H} = -\left(\hat{\sigma}_1^x \hat{\sigma}_2^x + \hat{\sigma}_1^y \hat{\sigma}_2^y\right) + \hat{\sigma}_1^z \hat{\sigma}_2^z + \hat{\sigma}_1^z + \hat{\sigma}_2^z \tag{4.8}$$

could be partitioned in the following ways:

1. $\{-\hat{\sigma}_1^x\hat{\sigma}_2^x\}, \{-\hat{\sigma}_1^y\hat{\sigma}_2^y\}, \{\hat{\sigma}_1^z\hat{\sigma}_2^z\}, \{\hat{\sigma}_1^z\}, \{\hat{\sigma}_2^z\},$

2. $\{-\hat{\sigma}_1^x\hat{\sigma}_2^x\}, \{-\hat{\sigma}_1^y\hat{\sigma}_2^y, \ \hat{\sigma}_1^z\hat{\sigma}_2^z\}, \{\hat{\sigma}_1^z, \ \hat{\sigma}_2^z\},$

3. $\{-\hat{\sigma}_1^x\hat{\sigma}_2^x, \ -\hat{\sigma}_1^y\hat{\sigma}_2^y, \ \hat{\sigma}_1^z\hat{\sigma}_2^z\}, \{\hat{\sigma}_1^z, \ \hat{\sigma}_2^z\}.$

When measuring the state $|\Psi\rangle = |01\rangle$, partition 1 has variance $\sum_{m=1}^{5}(\Delta\hat{R}_m)^2 = 2$ and $M = 5$ commuting sets for a total of $N^{(1)} = 10/\epsilon^2$ measurements [see Eq. (4.7)]. Partition 2 has the same variance because the operators within the sets have zero covariance, but here $M = 3$, so $N^{(2)} = 6/\epsilon^2$. Although partition 3 has only $M = 2$ commuting sets, the covariance between $\hat{\sigma}_1^x\hat{\sigma}_2^x$ and $\hat{\sigma}_1^y\hat{\sigma}_2^y$ adds to $(\Delta\hat{R}_1)^2$, giving $N^{(3)} = 8/\epsilon^2$ measurements. In this example, partition 2 gives the fewest number of measurements even though partition 3 has the fewest number of commuting sets.
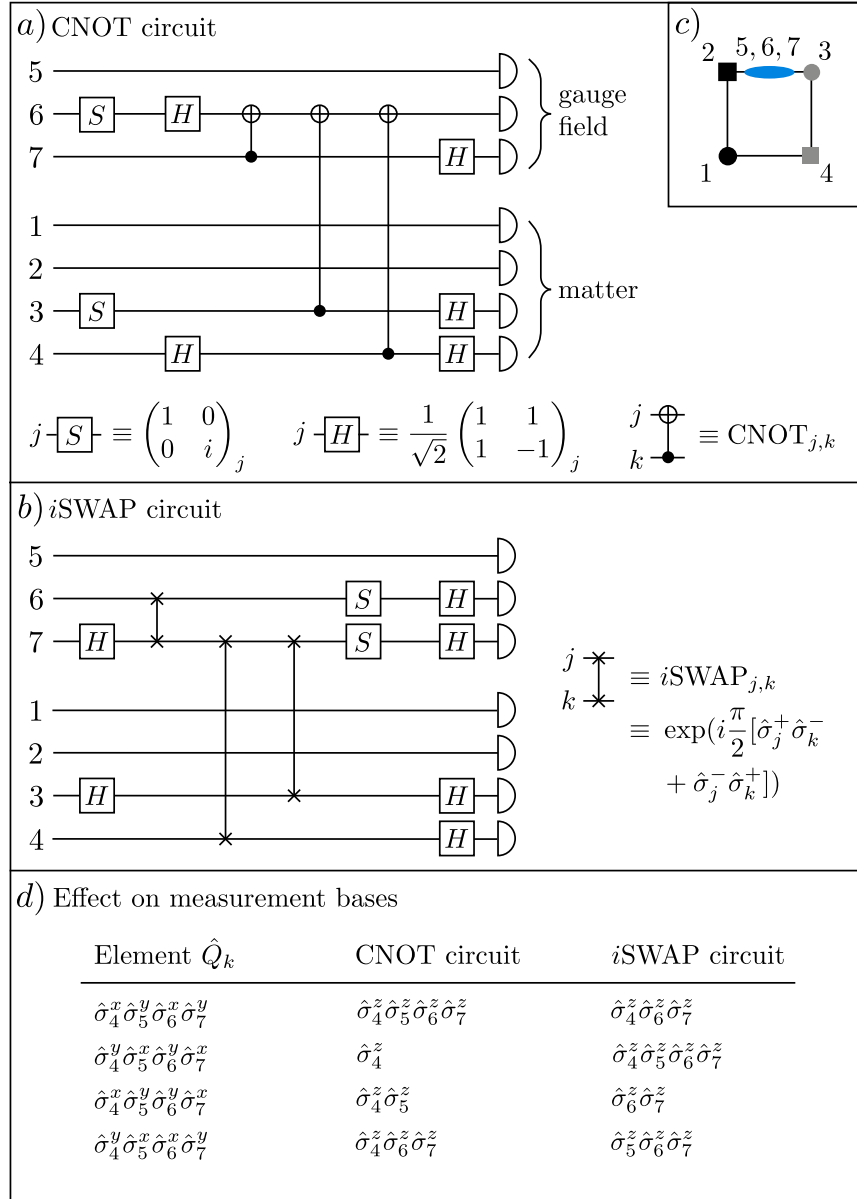
The variances and covariances of $\hat{Q}_k$ are dependent on the state $|\Psi\rangle$ being measured, which is generally unknown. Thus, to reduce the total number of measurements required, we seek a partitioning strategy that yields the minimum number of commuting sets, i.e. we minimize M without regard for the variance of the partitions.

The algorithm presented in Ref. [47] finds the partition of the $\hat{Q}_k$ into $\hat{R}_m$ that gives the near-minimum number of commuting sets M[1]. Although commuting operators can in principle be measured simultaneously, from an experimental point of view, only those operators which bitwise commute can be easily measured simultaneously with the local measurements provided by the quantum device. To exemplify this, consider $\hat{\sigma}_1^x\hat{\sigma}_2^x$ and $\hat{\sigma}_1^z\hat{\sigma}_2^z$. While these operators commute and thus can be simultaneously measured, there are no single qubit operations which rotate them into a diagonal form. To achieve this, two-qubit gates are required. Ref. [47] provides the procedure for building a quantum circuit which diagonalizes the Pauli operators $\hat{Q}_k$ within a commuting set (for an example, see Fig. 4.1). This circuit is to be placed after the VQE circuit and before the local measurements, effectively rotating the measurement basis and allowing us to measure in a complicated entangled basis. As such, all commuting operators within a commuting set, bitwise or not, can be measured simultaneously.

The gate set from which the quantum circuits are built can be adapted to suit the quantum computing platform, using for instance CNOT operations as entangling gates for superconducting platforms and iSWAP gates for ion-based platforms. While it is possible to express

---

[1]This is a greedy algorithm that scales well with the size of the system and the number of terms in the decomposition, but it is not guaranteed to find the optimal solution. It would be possible to develop an algorithm that finds the absolute minimum of M at the expense of additional computational resources.

a) CNOT circuit

gauge field

matter

$$ j-\boxed{S}- \equiv \begin{pmatrix} 1 & 0 \\ 0 & i \end{pmatrix}_j \qquad j-\boxed{H}- \equiv \frac{1}{\sqrt{2}} \begin{pmatrix} 1 & 1 \\ 1 & -1 \end{pmatrix}_j \qquad \begin{matrix} j \\ k \end{matrix} \equiv \mathrm{CNOT}_{j,k} $$

b) iSWAP circuit

$$ \begin{matrix} j \\ k \end{matrix} \equiv i\mathrm{SWAP}_{j,k} $$
$$ \equiv \exp(i\frac{\pi}{2}[\hat{\sigma}_j^+ \hat{\sigma}_k^- + \hat{\sigma}_j^- \hat{\sigma}_k^+]) $$

c)

d) Effect on measurement bases

Element $\hat{Q}_k$	CNOT circuit	iSWAP circuit
$\hat{\sigma}_4^x \hat{\sigma}_5^y \hat{\sigma}_6^x \hat{\sigma}_7^y$	$\hat{\sigma}_4^z \hat{\sigma}_5^z \hat{\sigma}_6^z \hat{\sigma}_7^z$	$\hat{\sigma}_4^z \hat{\sigma}_6^z \hat{\sigma}_7^z$
$\hat{\sigma}_4^y \hat{\sigma}_5^x \hat{\sigma}_6^y \hat{\sigma}_7^x$	$\hat{\sigma}_4^z$	$\hat{\sigma}_4^z \hat{\sigma}_5^z \hat{\sigma}_6^z \hat{\sigma}_7^z$
$\hat{\sigma}_4^x \hat{\sigma}_5^y \hat{\sigma}_6^y \hat{\sigma}_7^x$	$\hat{\sigma}_4^z \hat{\sigma}_5^z$	$\hat{\sigma}_6^z \hat{\sigma}_7^z$
$\hat{\sigma}_4^y \hat{\sigma}_5^x \hat{\sigma}_6^x \hat{\sigma}_7^y$	$\hat{\sigma}_4^z \hat{\sigma}_6^z \hat{\sigma}_7^z$	$\hat{\sigma}_5^z \hat{\sigma}_6^z \hat{\sigma}_7^z$

Figure 4.1: *An example of the measurement protocol explained in the main text, applied to the open boundary plaquette (see Sec. 2.2). The shown circuits diagonalize a measurements set $\hat{R}_m$ using CNOT gates (a) and iSWAP gates (b) as an entangling operation. The qubit labelling conventions are shown in (c). Applying the circuits before performing local measurements in a VQE protocol amounts to effectively performing measurements in an entangled basis. The table in (d) lists the elements $\hat{Q}_k$ in the chosen measurement set and their corresponding diagonalized elements using the CNOT circuit and the iSWAP circuit.*

a CNOT gate in terms of iSWAP gates, and vice versa, this leads to linear overhead in circuit depth, which can severely impact the feasibility of experiments with NISQ devices. Therefore, we adapt the algorithm in Ref. [47] according to the preferred type of two-qubit gate to avoid this linear overhead in the number of gates. As an example, Fig. 4.1(a) and 4.1(b) show two possible circuits which diagonalize one of the partitions $\hat{R}_m$ of the open boundary plaquette introduced in Sec. 2.2, with the qubit labelling convention shown in panel (c). The elements $\hat{Q}_k$ of this partition are shown in Fig. 4.1(d), along with the diagonal forms obtained after applying the CNOT and iSWAP circuits (for details Refs. [47, 48]).

In the worst-case scenario, the depth of the additional circuits scales quadratically with with the number of terms in the Pauli decomposition of the Hamiltonian K, however, in practice, we often see linear scaling. The computing time of the algorithm in Ref. [47] also scales quadratically in K, while the number of qubits in the system does not play a significant role in the complexity[2]. By applying this method to the Hamiltonians of Eqs. (2.6) and (2.7)-(2.8), we reduce the number of measurement sets (i.e. commuting sets) from 49 down to $M = 6$ for the open boundary plaquette. For the periodic boundary plaquette, the number of measurement sets is reduced from 295 to $M = 13$ for the electric representation (see Sec. 2.3) and from 138 down to $M = 9$ for the magnetic basis. The depth of the circuits used to implement the measurements is around ten in the worst-case scenario. We discuss generalizations beyond a single plaquette in Chap. 5.

---

[2]Although an increasing number of qubits brings the possibility of exponentially many decomposition terms K, in many physical scenarios, K is limited by the symmetries of the system, and we do not see exponential dependence.

Chapter 5

Implementations on a trapped ion quantum computer

So far, we described a framework for observing 2D effects in lattice gauge theories on quantum computers that can be implemented on any type of qubit-based device. In this section, we study the implementation of our approach on ion-based quantum computers. As explained in Sec. 5.1, ion-based quantum computers are well-suited to the models studied here. In Secs. 5.2 and 5.3, we present VQE protocols that are specific to trapped ion systems for the open boundary plaquette and periodic boundary plaquette, respectively. The VQE optimization routine is explained in Sec. 5.4.

5.1   VQE for ion-based quantum computers

As discussed in Chap. 4, we consider digital qubit-based approaches for the purpose of realizing proof-of-principle experiments with present-day technology. Promising quantum computing platforms include configurable Rydberg arrays [49, 50], superconducting architectures [51], and trapped ions [52, 53].

Rydberg-based approaches offer the advantage that 2D and 3D arrays can be realized using optical tweezers, which translates to a large number of available qubits. The ability to implement large qubit registers will make future generations of Rydberg arrays a very promising candidate for our schemes, once higher levels of controllability and gate fidelity become available. Superconducting and ion-based architectures offer both high controllability and gate fidelities already today. For superconducting qubits, entangling gates are

inherently of nearest-nearest neighbour type, which implies that entangling operations between non-neighbouring qubits have to be realized through a number of swap gates. While this is entirely possible, especially for next-generation devices, our models entail long-range interactions that result from the elimination of redundant gauge fields (see Secs. 2.2 and 2.3) and thus would require significant gate overhead on superconducting platforms. In contrast, ion-based quantum computers directly allow for addressed entangling gates between arbitrary qubits. This aligns well with our target models, motivating their use for this proposal.

Here, we consider a string of ions confined in a macroscopic linear Paul trap [52, 53]. The qubit states $|0\rangle$ and $|1\rangle$ are encoded in the electronic states of a single ion and can be manipulated using laser light in the visible spectrum. A universal set of quantum operations is available, which can be combined to implement arbitrary unitary operations. More specifically, the available gate-set consists of local rotations $\hat{U}_j(\phi) = \exp(-i\frac{\phi}{2}\hat{\sigma}_j^\alpha)$ and addressed Mølmer-Sørensen (MS) gates [54] between arbitrary pairs of qubits. These gates are implemented with fidelities exceeding 98% for both single- and multi-qubit gates [55–57]. Our VQE quantum circuits are adapted to these interactions and consist of NOT gates, parameterized single-qubit z-rotations, parameterized iSWAP gates, and parameterized controlled-iSWAP gates [defined in Fig. 5.1(b)]. As described in detail in the next sections, our circuits preserve the total magnetization $\hat{S}_{\text{tot}}^z = \sum_n \hat{\sigma}_n^z$ of the qubit register. This renders the quantum states robust with respect to collective dephasing, which is a dominant source of noise in trapped ion systems, thereby allowing the VQE to operate in a decoherence-free subspace [58].

While currently available ion-based hardware provides a sufficient number of qubits to carry our proposed protocols, future lattice gauge theory quantum simulations addressing larger lattices will require large-scale quantum devices. Ion-based quantum computers can be scaled up using networking approaches that connect several traps together [59] and therefore offer a pathway for developing quantum simulations of increasing size and complexity.

5.2 Open boundary conditions: dynamically generated magnetic fields

In this section, we show how to implement a VQE for the open boundary plaquette with dynamical matter [see Sec. 2.2]. As described in Sec. 3.1, the proposed experiment prepares the ground state of the effective Hamiltonian of Eqs. (2.6) and measures the ground state expectation value of the plaquette operator $\langle \Box \rangle$ to study the dynamical generation of gauge fields by pair creation processes. Using the qubit encoding given in Sec. 4.1, we provide a VQE circuit for this simulation. Furthermore, we present numerical results in which we classically simulate the proposed VQE protocol including noise.

The simulation involves four qubits for the matter fields (one for each site) and $2l + 1$ for the gauge field. Here, we consider $l = 1$ and thus the system consists of seven qubits. According to Fig. 4.1(c), we number the matter qubits as 1, 2, 3, and 4, and the gauge qubits 5, 6, and 7. Using the encoding given by Eq. (4.1), the gauge field basis states become

$$|1\rangle = |001\rangle, \tag{5.1a}$$
$$|0\rangle = |010\rangle, \tag{5.1b}$$
$$|-1\rangle = |100\rangle. \tag{5.1c}$$

The matter qubit states are given in Fig. 2.1(c). In the following, we will use the term "physical states" to refer to the computationally relevant qubit states. For the gauge fields,, this means that the qubit states lie in the computational space spanned by the states in Eqs. (5.1). For the matter fields, we operate in the zero-charge subsector (see Sec. 2.1), which translates into matter states of zero magnetization. For the open boundary plaquette, physical states have total magnetization $\langle \hat{S}_{\text{tot}}^z \rangle = 1$.
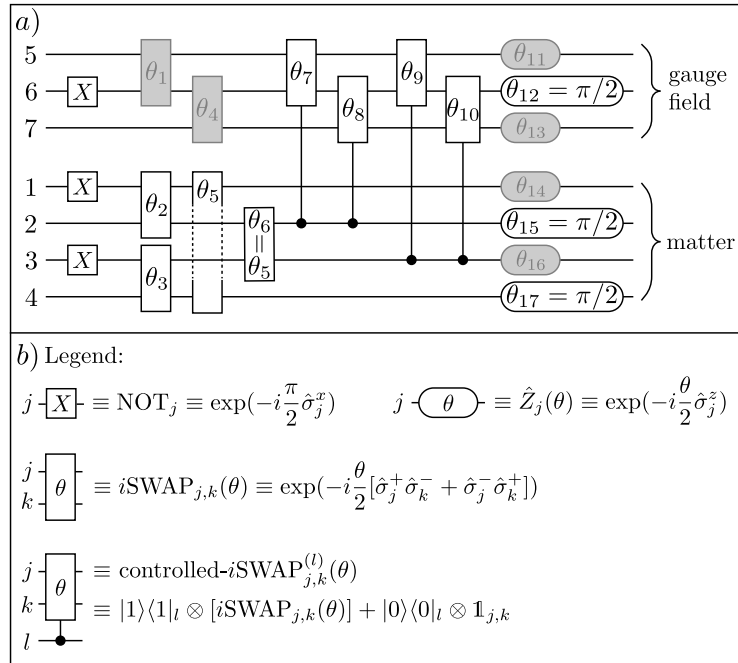
The gauge field operators are mapped according to Eqs. (4.2), giving

$$\hat{S}^z = \frac{1}{2}(\hat{\sigma}_5^z + \hat{\sigma}_5^z \hat{\sigma}_6^z), \tag{5.2a}$$
$$\hat{V}^- = \hat{\sigma}_5^- \hat{\sigma}_6^+ + \hat{\sigma}_6^- \hat{\sigma}_7^+. \tag{5.2b}$$

By inserting these expressions into Eqs. (2.6), the Hamiltonian can be written in terms of tensor products of Pauli operators.

The VQE quantum circuit shown in Fig. 5.1(a) preserves not only the total magnetization

Figure 5.1: *VQE circuit for preparing the ground state of a plaquette with open boundary conditions.* **(a)** *Quantum circuit with variational parameters θ_l shown for each gate. By identifying symmetries and redundancies via classical simulation, gates shaded in grey can be eliminated, and we set $\theta_6 = \theta_5$, $\theta_{12} = \theta_{15} = \theta_{17} = \pi/2$, leaving just seven variational parameters.* **(b)** *Definitions of the gates used.*

of the system, but also the magnetization of each of the gauge and matter subsystems. As mentioned in Sec. 4.1, our magnetization-preserving quantum circuit used in combination with physical input states confines the VQE to the space of physical states.

The VQE circuit in its unreduced form [i.e. including the grey-shaded gates in Fig. 5.1(a)] is motivated by the form of the Hamiltonian in Eqs. (2.6). All qubits are prepared in the input state $|0\rangle$, and NOT gates prepare the bare vacuum $|vvvv\rangle|0\rangle$ [see Fig. 2.1(c)] as the initial state for the VQE. The parameterized iSWAP gates are used to allow for all physical basis states within the matter and gauge subsystems. For the matter subsystem, there is a one-to-one correspondence between the iSWAP gates in the circuit and the terms comprising the kinetic Hamiltonian in Eq. (2.6d). These gates correspond to particle-antiparticle pair creation/annihilation in the model, and as a consequence, all matter basis states in the zero-charge subsector are made available by this part of the circuit. For the gauge field subsystem, the application of iSWAP gates allows for accessing all three gauge field states $|1\rangle$, $|0\rangle$, and $|-1\rangle$. Entanglement between the two subsystems is generated by a layer of parameterized controlled-iSWAP gates. In the effective Hamiltonian of Eqs. (2.6), the gauge degree of freedom lies on the $(2,3)$ link and is directly coupled to matter sites 2 and 3. Accordingly, the circuit couples the gauge field with only these two fermions, which act as controls in the layer of controlled-iSWAP gates. Finally, a layer of single-qubit z-rotations is applied to correct for relative phases, while other single-qubit operations are avoided as they are generally not magnetization preserving.

The quantum circuit described above allows for an exhaustive exploration of the physical subsector of the Hilbert space and involves a total of 17 variational parameters. While not strictly necessary, it is beneficial for currently available quantum hardware to reduce the number of variational parameters. This can be done by identifying the intrinsic symmetries of the ground state. By classically simulating the circuit in Fig. 5.1, we find that the solution space is still accessible by setting $\theta_6 = \theta_5$, fixing $\theta_{12} = \theta_{15} = \theta_{17} = \pi/2$, and removing the gates shaded in grey in Fig. 5.1(a), leaving a total of seven parameters.

Since the circuit design is based on the structure of the Hamiltonian, the same design principles can be applied to larger scale systems. For example, when adding more plaquettes, firstly, additional parametric iSWAP gates are used to allow for all basis states within the matter and gauge subsystems. Then, the gauge degrees of freedom are coupled to their respective neighbouring matter sites using additional controlled-iSWAP gates [in correspondence with Eq. (A.1)]. Finally, z-rotations adjust the relative phases of all qubits. When increasing the truncation l, additional iSWAP gates are inserted for populating the newly introduced gauge field states, and controlled-iSWAP gates for entangling them with

36

the respective matter sites are added. In both cases, adding more plaquettes and increasing the truncation cut-off, a linear increase in the number of qubits and iSWAP gates and a quadratic increase in the number of controlled-iSWAP operations is expected.
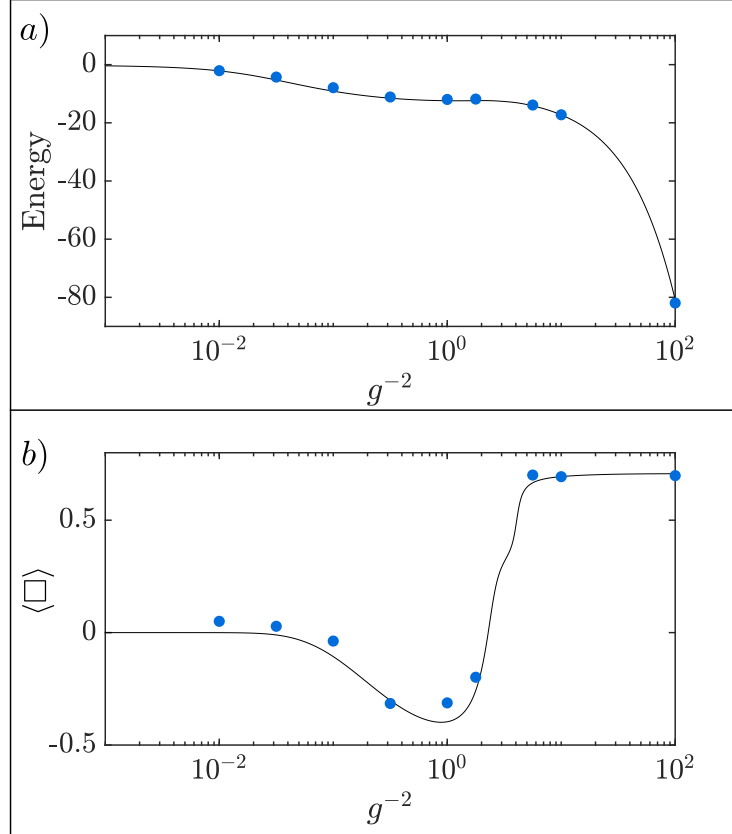
A classical simulation of the proposed experiment, including statistical noise on the cost function $\mathcal{C}(\boldsymbol{\theta})$, is shown in Fig. 5.2. The data points, shown by the blue dots, are post-selected based on energy from a set of multiple runs, i.e. we take the result with the lowest energy. The plaquette expectation value points are calculated using the exact state corresponding to the optimal variational parameters found by the VQE. The black solid lines are obtained via exact diagonalization of the Hamiltonian in Eqs. (2.6). Using the measurement procedure described in Sec. 4.3 and taking statistical error into account, the entire plot corresponds to approximately 4×10^7 measurements to be performed on the quantum device.

The energy of the variational ground state found by the VQE approximates well the energy of the exact ground state, as shown in Fig. 5.2(a). The plaquette expectation value is highly sensitive to small changes in the variational state, which leads to deviation with respect to the results obtained via exact diagonalization in Fig. 5.2(b), even for states whose energy is very close to the exact energy. The fidelity of the variational ground state with respect to the exact ground state is high in the extremal regions, i.e. greater than 98%, while all points achieve a fidelity exceeding 87%.

5.3   Periodic boundary conditions: running coupling

In this section, we provide a VQE protocol for simulating the running coupling in lattice gauge theories. As explained in Sec. 3.2, the running coupling is a genuine 2D effect that can be studied experimentally in a proof-of-concpet demonstration by first preparing the ground state of the periodic boundary plaquette and subsequently measuring the plaquette expectation value.

Differently from the open boundary plaquette, the electric and magnetic representations of the Hamiltonian [see Eqs. (2.7) and (2.8)] are used for different regions of the bare coupling g^{-2}. This is done to obtain better convergence to the full result without truncation, as the two representations are well suited for the strong and weak coupling regimes, respectively (see Sec. 2.3 and Ref. [22]). Using Eqs. (5.1) and (5.2) to encode the periodic boundary
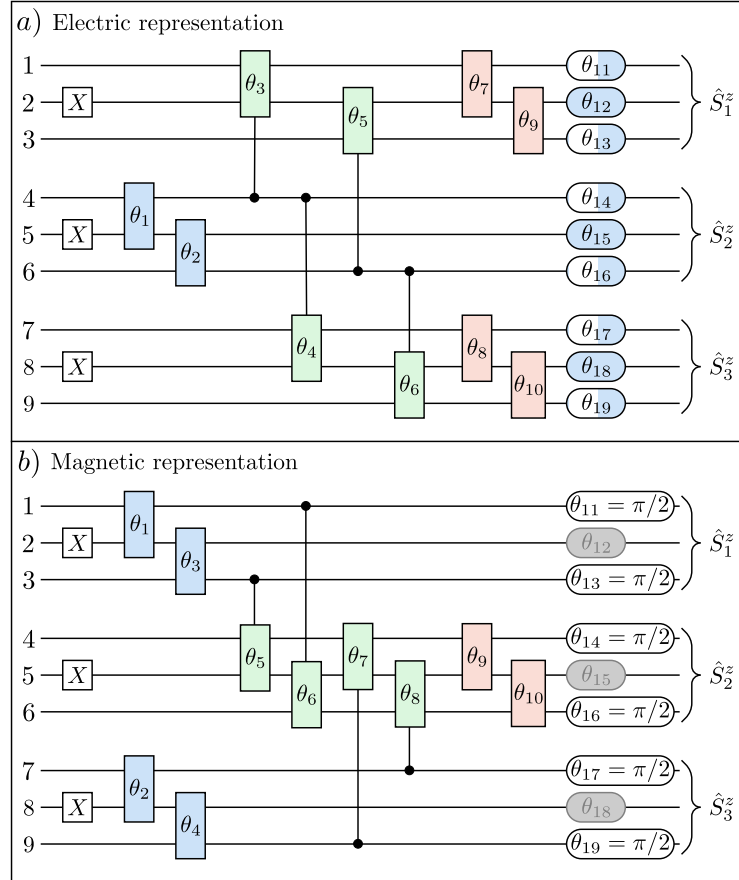
Figure 5.2: *Classical simulation of the proposed experiment for observing the dynamical generation of magnetic fields where $\Omega = 5$ and $m = 0.1$ (see Sec. 3.1) using the circuits given in Fig. 5.1. The blue dots represent data points post-selected based on energy from multiple runs. The black solid lines are determined via exact diagonalization of the Hamiltonians in Eqs. (2.6). **(a)** Energy of the variational ground state. **(b)** Plaquette expectation value $\langle \square \rangle$ as a function of g^{-2} calculated using the exact state corresponding to the optimal variational parameters found by the VQE.*

plaquette into nine qubits, rotator 1 is represented by qubits 1 through 3, rotator 2 by qubits 4 through 6, and rotator 3 by qubits 7 through 9 (see Fig. 5.3).

As for the open boundary plaquette, the circuit design for the periodic boundary plaquette is motivated by the structure of the system Hamiltonian and uses the trapped ion hardware-adapted gate set introduced in Sec. 5.1. Due to the differences between the electric and magnetic representations, we use two different VQE circuits which are shown in Fig. 5.3. Both circuits have 19 variational parameters and allow us to thoroughly explore the associated Hilbert spaces. However, since we are solely interested in the system ground state, it is convenient for NISQ technology to reduce the number of variational parameters by exploiting the symmetries between rotators 1 and 3 (which are apparent from the Hamiltonians) and by identifying additional redundant parameters through classical simulation of the VQE. As a result, in Fig. 5.3(a) we use a single parameter for each of the following sets: $\{\theta_1, \theta_2, \theta_{11}, \ldots, \theta_{19}\}$, $\{\theta_3, \ldots \theta_6\}$, and $\{\theta_7, \ldots, \theta_{10}\}$, as indicated by the colour coding. Parameters θ_{11}, θ_{13}, θ_{14}, θ_{16}, θ_{17}, and θ_{19} include an offset of $+\pi/2$ added to the shared variational parameter, which is indicated by the half-shaded gates. For the circuit in Fig. 5.3(b), we make the groupings $\{\theta_1, \theta_2, \theta_3, \theta_4\}$, $\{\theta_5, \ldots, \theta_8\}$, and $\{\theta_9, \theta_{10}\}$, while θ_{12}, θ_{15}, and θ_{18} can be eliminated, and θ_{11}, θ_{13}, θ_{14}, θ_{16}, θ_{17}, and θ_{19} are fixed at $\pi/2$. This leaves just three variational parameters for each circuit.

The circuit for the electric representation is shown in Fig. 5.3(a). All qubits are prepared in the input state $|0\rangle$, and NOT gates prepare the vacuum state $|0\rangle = |010\rangle$ for each of the three rotators as the intial state for the VQE. The layer of controlled-iSWAP gates reflects the coupling between the rotators in the electric Hamiltonian $\hat{H}_{\mathrm{E}}^{(\mathrm{e})}$ [see Eq. (2.7a)], which takes the form $-\hat{S}_2^z(\hat{S}_1^z + \hat{S}_3^z)$. This term results from the elimination of rotator 4 as a redundant degree of freedom, and introduces an asymmetry between rotator 2 and rotators 1 and 3. States in which all three rotators have the same sign ($|1\rangle|1\rangle|1\rangle$ and $|-1\rangle|-1\rangle|-1\rangle$) receive the strongest negative contribution from the coupling term $-\hat{S}_2^z(\hat{S}_1^z + \hat{S}_3^z)$, thus lowering the electric energy. To encourage the VQE to prepare states of this form, the parameterized controlled-iSWAP gates are connected to control the spread of population within rotators 1 and 3 based on the population of rotator 2.

The circuit for the magnetic representation of Eqs. (2.8) is shown in Fig. 5.3(b). Its construction is similar to the circuit for the electric representation described above, but rather encourages the flip-flop interactions between rotators described by $\hat{H}_{\mathrm{E}}^{(\mathrm{b})}$ [see Eq. (2.8a)]. Both the electric and magnetic circuits maintain constant magnetization of each gauge field, which prevents access to unphysical states.

39

Figure 5.3: *VQE circuits for preparing the ground state of a plaquette with periodic boundary conditions. Gate definitions are given in Fig. 5.1. Gates of the same colour in each circuit share a variational parameter after eliminating redundant parameters. The half-shaded gates include an offset of $+\pi/2$ added to the shared parameter, while the grey-shaded gates can be eliminated entirely. **(a)** Circuit for the electric representation of the Hamiltonian, and **(b)** for the magnetic representation.*
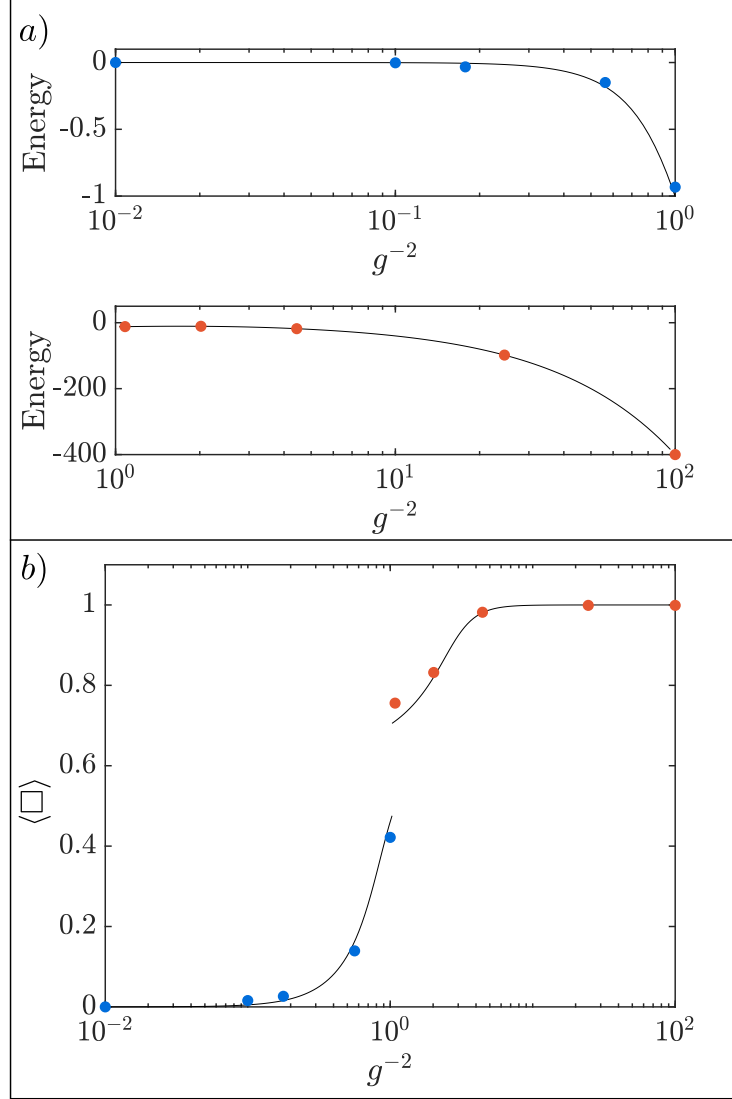
Figure 5.4: *Classical simulation of the proposed experiment for observing the running of the coupling (see Sec. 3.2) using the circuits given in Fig. 5.3. The data points are obtained from multiple runs via post-selection based on the lowest energy. The electric (magnetic) representation is shown in blue (red), and the black solid lines are determined via exact diagonalization of the Hamiltonians in Eqs. (2.7) and (2.8). **(a)** Energy of the variational ground state using the electric representation in the region $g^{-2} < 1$ and using the magnetic representation in the region $g^{-2} > 1$. **(b)** Plaquette expectation value $\langle \square \rangle$ as a function of g^{-2} calculated using the exact state corresponding to the optimal variational parameters found by the VQE.*

Designing the VQE circuit based on the form of the Hamiltonian allows for a scalable architecture. For systems with additional plaquettes, the coupling between rotators remains pairwise, which translates into the addition of controlled-iSWAP gates between all pairs of coupled gauge fields, as was described above for the open boundary plaquette. When considering larger truncations l, additional iSWAP gates are introduced to allow for all gauge field basis states. Additional controlled-iSWAP gates are then added to share entanglement in a similar fashion as for the case $l = 1$ considered here. In both cases, the scaling is the same as for the open boundary plaquette circuit, i.e. the number of qubits and the number of iSWAPs scale linearly, while the number of controlled-iSWAP gates scales quadratically in the worst-case scenario.

We simulate the proposed experiment classically, including statistical noise on the cost function $\mathcal{C}(\boldsymbol{\theta})$. Our results are shown in Fig. 5.4 and have been obtained via post-selection of the lowest energy result from multiple runs. Results using the electric and the magnetic representation of the Hamiltonian are shown in blue and red, respectively, while the black solid lines are obtained via exact diagonalization of the Hamiltonians. The plaquette expectation value data is calculated using the exact state obtained with the optimal variational parameters found by the VQE. Using the measurement procedure described in Sec. 4.3 and taking statistical error into account, the entire plot corresponds to 4×10^6 measurements to be performed on the quantum device.

The VQE protocol reaches the correct ground state energy [see Fig. 5.4(a)] and the expectation value of the plaquette operator in the variational ground state has good overlap with the exact truncated results, as shown in Fig. 5.4(b). The larger deviation of the plaquette operator expectation for $g^{-2} \ll 1$ can be attributed to the sensitivity of $\langle \Box \rangle$ with respect to the variational state in this parameter regime. More specifically, while the ground state for $g^{-2} \ll 1$ is the vacuum $|0\rangle|0\rangle|0\rangle$, slight changes in the variational parameters leave the energy nearly unchanged but have a bigger impact on the plaquette operator expectation value. The fidelity of the variational ground state with respect to the exact ground state is greater than 96% except for a small parameter window around $g^{-2} = 1$, where it is 93% in the worst case. We note that the fidelities around $g^{-2} = 1$ can be further improved by using a larger measurement budget to decrease the statistical noise on the cost function (see Sec. 4.3).

5.4   VQE optimization routine

In the following, we describe the classical optimization component of the VQE protocols used to obtain the numerical data shown in Figs. 5.2 and 5.4. The optimizer receives as input the outcome of the measurement of a variational state, and generates a new set of variational parameters $\boldsymbol{\theta}$ in an effort to minimize $\mathcal{C}(\boldsymbol{\theta})$, as described in Sec. 4.2.

One approach is to employ either exact or stochastic gradient-based optimization algorithms. However, the inherent probabilistic nature of quantum state measurements and the resulting statistical errors on the cost function $\mathcal{C}(\boldsymbol{\theta})$ pose a significant challenge for such techniques. Furthermore, methods to measure exact gradients of the cost function [60] are highly complex when applied to multi qubit gates and require additional ancilla qubits [61], while finite step size approximations of the gradient result in a large number of experimental evaluations. Additionally, the obtained gradient information is still stochastic, which requires modified descent methods such as Adam [62]. Alternatively, optimization with gradient-free techniques is feasible since the number of variational parameters in our proposals is relatively low (≤ 7).

We employ a combination of grid-based exploration of the parameter space and local optimization procedures for promising points. During the latter, when promising points are found, we fit a regression model in the form of a Gaussian process [63], which can either be used to perform traditional Bayesian optimization [64] or to provide a base to do a local search with gradient-based techniques. Simultaneously, the algorithm keeps track of parameter regions that are unexplored and favours those in later iterations by evaluating points on the predefined grid. At all times, the optimizer keeps track of a set of promising points which may be reevaluated if no new optimal points are found, or as a final step in the routine.

Furthermore, we define an interface between the classical optimizer and the quantum hardware, which stores the bare readouts and can hence reevaluate the data for variations in the cost function, e.g. when g^{-2} is modified. When the optimizer requests the evaluation of data points that have already been measured, the interface returns the corresponding data, but can also perform additional evaluations. The evaluations themselves are performed in a fashion that aims to minimize the statistical error of the samples. To be more precise, the interface automatically distributes the available measurement budget among the different commuting sets depending on their estimated variance. This leads to an overall reduction of the required budget, as it spares measurements of commuting partitions that have an

eigenstate close to the current state prepared by the quantum computer.

Chapter 6

Conclusions & outlook

In this work, we showed how to observe 2D effects in lattice gauge theories on currently available quantum computers. We used the new method presented in Ref. [22] to formulate 2D QED as an effective spin model with many-body interactions in a resource-efficient manner by eliminating redundant degrees of freedom. Importantly, this method provides a perspective for reaching the continuum limit of the considered gauge theory, and can be used for both classical and quantum simulations. Furthermore, we provided a practical framework based on VQE protocols to simulate these effective Hamiltonian descriptions using NISQ devices, including the numerics for observing 2D phenomena in a basic building block of 2D QED with present-day quantum resources.

The effective models studied here include both dynamical matter and a non-minimal gauge field truncation, providing the novel opportunity to study several 2D effects in lattice gauge theories. More specifically, we showed how to observe dynamical generation of magnetic fields and its interplay with particle-antiparticle pair creation, and paved the way for an important first step towards simulating short distance quantities such as the running coupling of QED. While the protocols presented in Chap. 5 are designed for trapped ion systems, our approach can be easily adapted to suit different types of quantum hardware.

One of the most appealing characteristics of our approach is that it can be generalized to more complex systems. Immediate extensions of our results include simulations of a 2D plane of multiple plaquettes, and of QED in three spatial dimensions. Moreover, including fermionic matter in the case of periodic boundary conditions can be done by following the same procedure as for open boundary conditions [22]. It will also be interesting to explore implementations on non-qubit based hardware that is capable of representing gauge de-

grees of freedom with spin-l systems ($l > 1/2$) [31]. As part of the quest to move towards quantum simulations of QCD, another possible extension is to progress from a U(1) gauge theory (QED) to a non-Abelian gauge theory, such as SU(2), and eventually to SU(3). Importantly, simulations of lattice gauge theories with larger lattice sizes will become feasible with future advancements in quantum computing, allowing for exciting possibilities, such as the ability to relate the running coupling of a gauge theory to a physical parameter and to make connections between quantum simulations and experiments in high energy physics. Ultimately, future quantum computers may offer the potential to also simulate models with a topological term, non-zero chemical potential, or real-time phenomena, effects which are very hard or even impossible to access with MCMC techniques.

The field of quantum simulations of lattice gauge theories is in its early exploratory stages and is rapidly developing. By providing practical and experimentally feasible solutions for simulating gauge theories beyond 1D, our work opens up new pathways towards accessing regimes that are classically out of reach.

References

[1] S. Aoki, Y. Aoki, D. Bečirević, T. Blum, G. Colangelo, *et al.*, Eur. Phys. J. C **80**, 1 (2020).

[2] S. Aoki, Y. Aoki, D. Bečirević, C. Bernard, T. Blum, *et al.*, Eur. Phys. J. C **77**, 112 (2017).

[3] M. Troyer and U.-J. Wiese, Phys. Rev. Lett. **94**, 170201 (2005).

[4] C. Gattringer and K. Langfeld, Int. J. Mod. Phys. A **31**, 1643007 (2016).

[5] M. Bañuls, K. Cichy, I. Cirac, K. Jansen, and S. Kühn, Bull. Am. Phys. Soc. **63** (2018).

[6] M. C. Bañuls and K. Cichy, Rep. Prog. Phys. **83**, 024401 (2020).

[7] A. Mil, T. V. Zache, A. Hegde, A. Xia, R. P. Bhatt, *et al.*, Science **367**, 1128 (2020).

[8] E. A. Martinez, C. A. Muschik, P. Schindler, D. Nigg, A. Erhard, *et al.*, Nature **534**, 516 (2016).

[9] C. Muschik, M. Heyl, E. Martinez, T. Monz, P. Schindler, *et al.*, New J. Phys. **19**, 103020 (2017).

[10] N. Klco, E. F. Dumitrescu, A. J. McCaskey, T. D. Morris, R. C. Pooser, *et al.*, Phys. Rev. A **98**, 032331 (2018).

[11] N. Klco, M. J. Savage, and J. R. Stryker, Phys. Rev. D **101**, 074512 (2020).

[12] M. C. Bañuls, R. Blatt, J. Catani, A. Celi, J. I. Cirac, *et al.*, arXiv:1911.00003 .

[13] C. Kokail, C. Maier, R. van Bijnen, T. Brydges, M. K. Joshi, *et al.*, Nature **569**, 355 (2019).

[14] C. Schweizer, F. Grusdt, M. Berngruber, L. Barbiero, E. Demler, *et al.*, Nat. Phys. **15**, 1168 (2019).

[15] F. Görg, K. Sandholzer, J. Minguzzi, R. Desbuquois, M. Messer, *et al.*, Nat. Phys. **15**, 1161 (2019).

[16] B. Yang, H. Sun, R. Ott, H.-Y. Wang, T. V. Zache, *et al.*, arXiv:2003.08945 .

[17] A. Celi, B. Vermersch, O. Viyuela, H. Pichler, M. D. Lukin, *et al.*, Phys. Rev. X **10**, 021057 (2020).

[18] E. Zohar, J. I. Cirac, and B. Reznik, Phys. Rev. A **88** (2013), 10.1103/physreva.88.023617.

[19] D. González-Cuadra, E. Zohar, and J. I. Cirac, New J. Phys. **19**, 063038 (2017).

[20] C. Hamer, J. Kogut, D. Crewther, and M. Mazzolini, Nucl. Phys. B **208**, 413 (1982).

[21] C. Hamer, Z. Weihong, and J. Oitmaa, Phys. Rev. D **56**, 55 (1997).

[22] J. F. Haase, L. Dellantonio, A. Celi, D. Paulson, A. Kan, *et al.*, arXiv:2006.14160 .

[23] J. Preskill, Quantum **2**, 79 (2018).

[24] J. R. McClean, J. Romero, R. Babbush, and A. Aspuru-Guzik, New J. Phys. **18**, 023023 (2016).

[25] O. Shehab, I. H. Kim, N. H. Nguyen, K. Landsman, C. H. Alderete, *et al.*, arXiv:1906.00476 .

[26] F. Arute, K. Arya, R. Babbush, D. Bacon, J. C. Bardin, *et al.*, Nature **574**, 505 (2019).

[27] D. Ghosh, P. Agarwal, P. Pandey, B. K. Behera, and P. K. Panigrahi, Quantum Inf. Process. **17**, 153 (2018).

[28] M. Creutz, L. Jacobs, and C. Rebbi, Phys. Rep. **95**, 201 (1983).

[29] J. Kogut and L. Susskind, Phys. Rev. D **11**, 395 (1975).

[30] K. G. Wilson, Phys. Rev. D **10**, 2445 (1974).

[31] C. Senko, P. Richerme, J. Smith, A. Lee, I. Cohen, *et al.*, Phys. Rev. X **5**, 021026 (2015).

[32] P. Jordan and E. P. Wigner, Z. Phys. **47**, 631 (1928).

[33] C. Gattringer and C. B. Lang, Lect. Notes Phys. **788**, 1 (2010).

[34] L. Funcke, K. Jansen, and S. Kühn, Phys. Rev. D **101**, 054507 (2020).

[35] E. H. Lieb, Phys. Rev. Lett. **73**, 2158–2161 (1994).

[36] S. Booth, M. Göckeler, R. Horsley, A. Irving, B. Joo, *et al.*, Phys. Lett. B **519**, 229 (2001).

[37] M. E. Peskin and D. V. Schroeder, *An Introduction to quantum field theory* (Addison-Wesley, Reading, USA, 1995).

[38] M. Bruno, M. Dalla Brida, P. Fritzsch, T. Korzec, A. Ramos, *et al.*, Phys. Rev. Lett. **119**, 102001 (2017).

[39] S. P. Jordan, K. S. M. Lee, and J. Preskill, Science **336**, 1130–1133 (2012).

[40] P. J. O'Malley, R. Babbush, I. D. Kivlichan, J. Romero, J. R. McClean, *et al.*, Phys. Rev. X **6**, 031007 (2016).

[41] C. Hempel, C. Maier, J. Romero, J. McClean, T. Monz, *et al.*, Phys. Rev. X **8**, 031022 (2018).

[42] A. Peruzzo, J. McClean, P. Shadbolt, M.-H. Yung, X.-Q. Zhou, *et al.*, Nat. Commun. **5**, 4213 (2014).

[43] E. F. Dumitrescu, A. J. McCaskey, G. Hagen, G. R. Jansen, T. D. Morris, *et al.*, Physical review letters **120**, 210501 (2018).

[44] O. Shehab, K. Landsman, Y. Nam, D. Zhu, N. M. Linke, *et al.*, Phys. Rev. A **100**, 062319 (2019).

[45] E. Farhi, J. Goldstone, and S. Gutmann, arXiv:1411.4028 .

[46] N. Moll, P. Barkoutsos, L. S. Bishop, J. M. Chow, A. Cross, *et al.*, Quantum Sci. Technol. **3**, 030503 (2018).

[47] A. Jena, S. Genin, and M. Mosca, arXiv:1907.07859 .

[48] A. Jena, *et al.*, In preparation.

[49] H. Bernien, S. Schwartz, A. Keesling, H. Levine, A. Omran, *et al.*, Nature **551**, 579 (2017).

[50] H. Labuhn, D. Barredo, S. Ravets, S. De Léséleuc, T. Macrì, *et al.*, Nature **534**, 667 (2016).

[51] A. D. Córcoles, E. Magesan, S. J. Srinivasan, A. W. Cross, M. Steffen, *et al.*, Nat. Commun. **6**, 1 (2015).

[52] B. P. Lanyon, C. Hempel, D. Nigg, M. Müller, R. Gerritsma, *et al.*, Science **334**, 57 (2011).

[53] S. Debnath, N. M. Linke, C. Figgatt, K. A. Landsman, K. Wright, *et al.*, Nature **536**, 63 (2016).

[54] A. Sørensen and K. Mølmer, Phys. Rev. Lett. **82**, 1971 (1999).

[55] J. Benhelm, G. Kirchmair, C. F. Roos, and R. Blatt, Nat. Phys. **4**, 463 (2008).

[56] K. R. Brown, A. C. Wilson, Y. Colombe, C. Ospelkaus, A. M. Meier, *et al.*, Phys. Rev. A **84**, 030303 (2011).

[57] J. Zhang, G. Pagano, P. W. Hess, A. Kyprianidis, P. Becker, *et al.*, Nature **551**, 601 (2017).

[58] P. Schindler, D. Nigg, T. Monz, J. T. Barreiro, E. Martinez, *et al.*, New J. Phys. **15**, 123012 (2013).

[59] C. Monroe, R. Raussendorf, A. Ruthven, K. R. Brown, P. Maunz, *et al.*, Phys. Rev. A **89**, 022317 (2014).

[60] J. Li, X. Yang, X. Peng, and C.-P. Sun, Phys. Rev. Lett. **118**, 150503 (2017).

[61] M. Schuld, V. Bergholm, C. Gogolin, J. Izaac, and N. Killoran, Phys. Rev. A **99**, 032331 (2019).

[62] D. P. Kingma and J. Ba, arXiv:1412.6980 .

[63] C. E. Rasmussen, in *Summer School on Machine Learning* (Springer, 2003) pp. 63–71.

[64] P. I. Frazier, arXiv:1807.02811 .

Appendix A

Effective Hamiltonian for a ladder of plaquettes with open boundary conditions

In this appendix, we derive an expression for the electric term in the Hamiltonian in Eq. (2.2) for a ladder of N plaquettes [see Fig. 2.1(a)]. Following the procedure outlined in Sec. 2.2, we implement Gauss' law to remove redundant gauge degrees of freedom and obtain an expression with only the independent gauge fields remaining. We then use the Jordan-Wigner transformation and the mapping in Eqs. (2.4) to arrive at the final Hamiltonian for the ladder. The magnetic, mass, and kinetic terms remain unchanged, except for the identity operators where the degrees of freedom are removed.

To write the electric term $\hat{H}_{\mathrm{E}}$ in Eqs. (2.2), we express the electric field on each link in terms of the chosen independent gauge and matter degrees of freedom (see Sec. 2.1). Categorizing links according to their orientation and location [defined in Fig. 2.1(a)], we examine the following cases: horizontal independent links, horizontal dependent links, outermost vertical links, and internal vertical links. Listed in Table A.1 are the electric field contributions of each of these terms for even- and odd-numbered plaquettes, written in terms of the horizontal independent links.

Squaring each contribution in Table A.1 and summing over the plaquettes allows us to arrive at an expression for the electric term in terms of only the independent gauge fields. Using the Jordan-Wigner transformation and Eqs. (2.4)-(2.5), the Hamiltonian for the

Link type	Even plaquette n	Odd plaquette k
Horizontal independent	$\hat{E}_{2n,2n+1}$	$\hat{E}_{2k,2k+1}$
Horizontal dependent	$\hat{E}_{2n-1,2n+2} = -\hat{E}_{2n,2n+1} - \sum_{i=1}^{2n} \hat{q}_i$	$\hat{E}_{2k-1,2k+2} = \hat{E}_{2n-1,2n+2}$
Vertical outermost	$\hat{E}_{12} = \hat{E}_{23} + \hat{q}_2$ $\hat{E}_{2N+1,2N+2} = \hat{E}_{2N,2N+1} - \hat{q}_{2N+1}$	$\hat{E}_{12} = \hat{E}_{23} + \hat{q}_2$ $\hat{E}_{2N+2,2N+1} = -\hat{E}_{2N+1,2N+2}$
Vertical internal	$\hat{E}_{2n+1,2n+2} = \hat{E}_{2n,2n+1} + \hat{E}_{2n+2,2n+3}$ $+ \sum_{i=1}^{2n} \hat{q}_i - \hat{q}_{2n+2}$	$\hat{E}_{2k+2,2k+1} = -\hat{E}_{2n+1,2n+2}$

Table A.1: *Electric field of each link in the ladder of Fig. 2.1(a). For the vertical outermost links, the cases of "even" and "odd" refer to the total number of plaquettes N.*

ladder can then be written

$$\hat{H} = \hat{H}_{\mathrm{E}} + \hat{H}_{\mathrm{B}} + \hat{H}_{\mathrm{m}} + \hat{H}_{\mathrm{kin}}, \tag{A.1a}$$

$$\hat{H}_{\mathrm{E}} = \frac{g^2}{2} \Big\{ \sum_{n=1}^{N} \Big[\big(\hat{S}_{2n,2n+1}^z \big)^2 + \Big(\hat{S}_{2n,2n+1}^z + \sum_{i=1}^{2n} \hat{q}_i \Big)^2 \Big]$$
$$+ \sum_{n=1}^{N-1} \Big[\hat{S}_{2n,2n+1}^z + \hat{S}_{2n+2,2n+3}^z + \sum_{i=1}^{2n} \hat{q}_i + \hat{q}_{2n+2} \Big]^2$$
$$+ \Big[\hat{S}_{23}^z + \hat{q}_2 \Big]^2 + \Big[\hat{S}_{2N,2N+1}^z - \hat{q}_{2N+1} \Big]^2 \Big\} \tag{A.1b}$$

$$\hat{H}_{\mathrm{B}} = -\frac{1}{2g^2} \sum_{n=1}^{N} \Big(\hat{V}_{2n,2n+1}^- + \hat{V}_{2n,2n+1}^+ \Big), \tag{A.1c}$$

$$\hat{H}_{\mathrm{m}} = \frac{m}{2} \sum_{i=1}^{2N+2} (-1)^{i+1} \hat{\sigma}_i^z, \tag{A.1d}$$

$$\hat{H}_{\mathrm{kin}} = -i\Omega \Big[\hat{\sigma}_1^+ \hat{\sigma}_2^- + \sum_{n=1}^{N} \Big(\hat{\sigma}_{2n}^- \hat{V}_{2n,2n+1}^+ \hat{\sigma}_{2n+1}^+ + (-1)^n (\hat{\sigma}_{2n+1}^+ \hat{\sigma}_{2n+2}^-)$$
$$- \hat{\sigma}_{2n-1}^+ \hat{\sigma}_{2n}^z \hat{\sigma}_{2n+1}^z \hat{\sigma}_{2n+2}^- \Big) \Big] + \mathrm{H.c.}, \tag{A.1e}$$

where $\hat{\sigma}_i^\pm = \frac{1}{2}(\hat{\sigma}_i^x \pm \hat{\sigma}_i^y)$ and $\hat{\sigma}_i^x, \hat{\sigma}_i^y, \hat{\sigma}_i^z$ are the Pauli operators acting on the ith qubit. Here, the charge operator $\hat{q}_i$ under the Jordan-Wigner transformation becomes $\hat{q}_i = \frac{Q}{2}\left(\hat{\sigma}_i^z + (-1)^{i+1}\right)$.

Appendix B

Perturbation theory

In this appendix, we outline the perturbative algorithm used to determine the analytical results presented in Sec. 3.1.

We consider the system Hamiltonian to be $\hat{H} = \hat{H}_0 + \hat{H}_{\text{kin}}$, where $\hat{H}_0 = \hat{H}_{\text{E}} + \hat{H}_{\text{m}}$ [see Eqs (2.6a) and (2.6c)] is the bare Hamiltonian and $\hat{H}_{\text{kin}}$ [see Eq. (2.6d)] is the perturbation. Following standard perturbation theory, the corrected state and energy for eigenvalue i up to order n can be written as

$$|\Psi_i\rangle = \sum_{j=0}^{n} |\Psi_i^{(j)}\rangle, \tag{B.1a}$$

$$E_i = \sum_{j=0}^{n} E_i^{(j)}. \tag{B.1b}$$

The unperturbed state $|\Psi_i^{(0)}\rangle$ can be any of the eigenstates of $\hat{H}_0$. Our goal is to find the corrections for $j \geq 1$ in Eqs. (B.1) up to an arbitrary order and for any initial state. We require higher orders in perturbation theory because the leading and the second leading contributions are found at fourth and sixth orders, respectively. Furthermore, degeneracies in our system are often lifted at fourth order.

The eigenstates and corresponding eigenvalues of the bare Hamiltonian $\hat{H}_0$ are denoted as $|\Psi_{i,\mu}^{(0)}\rangle$ and $E_i^{(0)}$, where μ is an index used within the degenerate subspace that contains the unperturbed state $|\Psi_i^{(0)}\rangle$. As an example, the six lowest energy eigenstates of $\hat{H}_0$ are as follows (see Fig. B.1): the non-degenerate vacuum state $|vvvv\rangle|0\rangle$ with null energy; the

four-fold degenerate two-particle states $|epvv\rangle|0\rangle$, $|vpev\rangle|1\rangle$, $|vvep\rangle|0\rangle$, and $|evvp\rangle|0\rangle$, each with energy $\frac{g^2}{2}+2m$; and the two-fold degenerate fully-filled plaquette states $|epep\rangle|0\rangle$ and $|epep\rangle|1\rangle$, each with energy g^2+4m [see Fig. 2.1(e)].

Acting on an eigenstate of $\hat{H}_0$ with the kinetic term creates and annihilates particle-antiparticle pairs, and fixes the field on the links to satisfy Gauss' law. Successive applications of $\hat{H}_{\text{kin}}$ on the vacuum are shown in Fig. B.1. This illustration shows that acting $\hat{H}_{\text{kin}}$ on a state an odd number of times results in a state that is orthogonal to the initial state, implying that odd order perturbative energy corrections are vanishing (see Eq. (B.2b)).

At the beginning of our algorithm, the initial state $|\Psi_i^{(0)}\rangle$ is set to an unknown superposition of states within the selected eigensubspace i, i.e. $|\Psi_i^{(0)}\rangle = \sum_\nu d_\nu^{(0)}|\Psi_{i,\nu}^{(0)}\rangle$. If the subspace i is degenerate, the coefficients $d_\nu^{(0)}$ are determined by lifting – when possible – the degeneracy at higher orders (see below). The nth order perturbative corrections are calculated as

$$\langle\Psi_k^{(0)}|\Psi_i^{(n)}\rangle = \frac{\langle\Psi_k^{(0)}|\hat{V}|\Psi_i^{(n-1)}\rangle}{E_i^{(0)}-E_k^{(0)}} - \sum_{j=1}^{n-1} E_i^{(j)}\frac{\langle\Psi_k^{(0)}|\Psi_i^{(n-j)}\rangle}{E_i^{(0)}-E_k^{(0)}}, \tag{B.2a}$$

$$E_i^{(n)} = \langle\Psi_i^{(0)}|\hat{V}|\Psi_i^{(n-1)}\rangle - \sum_{j=1}^{n-1} E_i^{(j)}\langle\Psi_i^{(j)}|\Psi_i^{(n-j)}\rangle, \tag{B.2b}$$

$$\langle\Psi_{i,\nu}^{(0)}|\Psi_i^{(n)}\rangle = d_\nu^{(n)}, \tag{B.2c}$$

where $|\Psi_k^{(0)}\rangle$ with energy $E_k^{(0)}$ are the eigenstates of $\hat{H}_0$ outside the degenerate eigensubspace which contains the initial state. The overlap $d_\nu^{(n)}$ of the state correction with the eigenstates $|\Psi_{i,\nu}^{(0)}\rangle$ within the same degenerate subspace can be determined by imposing normalization when the degeneracy is lifted. The specific form of Eqs. (B.2) follows from the symmetries that our perturbation H_{kin} satisfies. In particular, $E_i^{(n)} = d_\nu^{(n)} = 0$ for odd n.

To lift a degeneracy, the coefficients $d_\nu^{(0)}$ need to be found by diagonalizing the matrix equation

$$\langle\Psi_{i,\nu}^{(0)}|\hat{V}|\Psi_i^{(n-1)}\rangle = \sum_{j=2}^n E_i^{(j)}\langle\Psi_{i,\nu}^{(0)}|\Psi_i^{(n-j)}\rangle. \tag{B.3}$$

55

Energy		0th order	$\hat{H}_{\text{kin}}$	1st order	$\hat{H}_{\text{kin}}$	2nd order	$\hat{H}_{\text{kin}}$	3rd order
	$\frac{3g^2}{2}+2m$							$|evvp\rangle|-1\rangle$ $|vpev\rangle|0\rangle$
	g^2+4m					$|epep\rangle|0\rangle$		
	$\frac{g^2}{2}+2m$			$|vvep\rangle|0\rangle$ $|epvv\rangle|0\rangle$				$|vvep\rangle|0\rangle$ $|epvv\rangle|0\rangle$
	0	$|vvvv\rangle|0\rangle$				$|vvvv\rangle|0\rangle$		
	$\frac{g^2}{2}+2m$			$|evvp\rangle|0\rangle$ $|vpev\rangle|1\rangle$				$|evvp\rangle|0\rangle$ $|vpev\rangle|1\rangle$
	g^2+4m					$|epep\rangle|1\rangle$		
	$\frac{3g^2}{2}+2m$							$|vvep\rangle|1\rangle$ $|epvv\rangle|1\rangle$

Figure B.1: *Schematic description of our perturbative algorithm when starting from the vacuum. In the first column, we show the bare energies of the corresponding states. Each application of the perturbation $\hat{H}_{kin}$ allows for creating and annihilating particle-antiparticle pairs, as depicted by the tree structure. At each iteration, our algorithm expands the Hilbert space to include new terms contributing to the correction. This allows for efficiently using the resources, ultimately reaching several hundred orders in perturbation theory.*

Eq. (B.3) can only be solved at the order m at which the perturbation lifts the degeneracy. For instance, when starting from the fully-filled plaquette states $|epep\rangle|0\rangle$ and $|epep\rangle|1\rangle$, the two-fold degeneracy is lifted at $m = 4$. On the other hand, the four-fold degeneracy between the two-particle states is only partially lifted at $m = 2$ into two two-fold degenerate systems $\{|evvp\rangle|0\rangle, |vpev\rangle|1\rangle\}$ and $\{|epvv\rangle|0\rangle, |vvep\rangle|0\rangle\}$. The former is fully lifted at $m = 4$. The latter remains degenerate for all orders because these states satisfy the same symmetry as the perturbation $\hat{H}_{\text{kin}}$.

As mentioned in Sec. 3.1, the jump coordinate g_{c} can be estimated using perturbation theory. The jump occurs when the ground state transitions from $|f_-\rangle$ to $|f_+\rangle$ (see Sec. 3.1), i.e. when the energies of the two states are equal. Given that the bare energies $E_i^{(0)}$ are the same, this means that for $g = g_{\text{c}}$ the sum of the kinetic E_{kin} and magnetic $E_{\text{B}} = -\langle\square\rangle/(2g^2)$ energies for the two states are equal. While E_{kin} is the energy correction given from perturbation theory, one can determine E_{B} using the corrected state $|\Psi_i\rangle = |f_\pm\rangle$. Thus, we can write $E_{\text{B}}^{(+)} + E_{\text{kin}}^{(+)} = E_{\text{B}}^{(-)} + E_{\text{kin}}^{(-)}$, where the superscript $(\pm)$ indicates the perturbative

state $|f_\pm\rangle$ used. By solving for g, we arrive at the estimated jump coordinate up to order n in perturbation theory.

Appendix C

Ground state of open boundary plaquette for weak coupling

In this appendix, we derive the ground state of the open boundary plaquette in the weak coupling regime of $g^{-2} \gg 1$. The following derivations are valid for the non-perturbative regime described in Sec. 3.1 [see Fig. 3.2(d)], where $\Omega \gg |m|$ and $\Omega \ll g^{-2}$. The Hamiltonian is given in Eqs. (2.2).

For large g^{-2}, the Hamiltonian is dominated by the magnetic term $\hat{H}_\mathrm{B}$, which contains only gauge field operators. As such, the ground state is required to be a product state between some matter configuration and ground state of the magnetic term. This is confirmed by the plot of the entanglement entropy in Fig. 3.2(a), which shows that the ground state is separable between matter and gauge components for large g^{-2}. Therefore, we set the ground state to be a tensor product $|\Psi\rangle = |\psi\rangle|\mathrm{GS}^{(b)}\rangle$ between some matter configuration $|\psi\rangle = \sum_{j=1}^{6} c_j |m_j\rangle$ and the ground state of the magnetic term $|\mathrm{GS}^{(b)}\rangle$. Here, $|m_j\rangle$ are the allowed matter configurations $\{|vvvv\rangle, |epvv\rangle, |vpev\rangle, |vvep\rangle, |evvp\rangle, |epep\rangle\}$ for $j = 1,\ 2,\ldots,\ 6$, respectively (see Table C.1). While the magnetic term is dominant, it does not influence the matter configuration. For simplicity, we set the mass $m = 0$ (the following procedure can be generalized for non-zero m), leaving the remaining candidates for determination of the matter state to be $\hat{H}_\mathrm{E}$ and $\hat{H}_\mathrm{kin}$. We are in the limit $\Omega \gg 1$, $g^{-2} \gg 1$, and so the kinetic term is dominant over the electric term. By minimizing $\langle\Psi|\hat{H}_\mathrm{kin}|\Psi\rangle$ over the c_j, we can estimate the matter component of the ground state at large g^{-2}.

j	$|m_j\rangle$	c_j $(l = 1)$	c_j $(l \to \infty)$
1	$|vvvv\rangle$	$-0.50i$	$-i/2$
2	$|epvv\rangle$	0.49	$1/2$
3	$|vpev\rangle$	-0.073	0
4	$|vvep\rangle$	-0.49	$-1/2$
5	$|evvp\rangle$	0.073	0
6	$|epep\rangle$	$-0.50i$	$-i/2$

Table C.1: *The c_j for different truncations obtained from minimizing Eq. (C.1) which correspond to the matter component of the ground state of the open boundary plaquette Hamiltonian for large g^{-2}.*

The expression for $\langle\Psi|\hat{H}_{\mathrm{kin}}|\Psi\rangle$ can be written as

$$
\langle\Psi|\hat{H}_{\mathrm{kin}}|\Psi\rangle = i\Omega\Big(c_1^* c_2 + c_1^* c_5 + c_3^* c_6 + c_4^* c_1 + c_4^* c_6 + c_6^* c_2
$$
$$
+ \big(c_1^* c_3 + c_5^* c_6\big)\langle\mathrm{GS}^{(b)}|\hat{V}^-|\mathrm{GS}^{(b)}\rangle\Big) + \mathrm{H.c.}, \tag{C.1}
$$

and the optimal c_j are shown in Table C.1 for truncation $l = 1$ and $l \to \infty$. The residual probabilities of the states $|vpev\rangle$ and $|evvp\rangle$ in Fig. 3.2(d) are an effect of the $l = 1$ truncation. Constructing the estimated ground state $|\Psi\rangle = |\psi\rangle|\mathrm{GS}^{(b)}\rangle$ using the optimal c_j, we find that $|\Psi\rangle$ has over 99.9% overlap with the ground state obtained via exact diagonalization of the Hamiltonian in Eqs. (2.2) for large g^{-2}.